JCI The Journal of Clinical Investigation

Modulation of NOX2 causes obesity-mediated atrial fibrillation

Arvind Sridhar, … , Jalees Rehman, Dawood Darbar

J Clin Invest. 2024. https://doi.org/10.1172/JCI175447.

Research In-Press Preview Cardiology

Graphical abstract

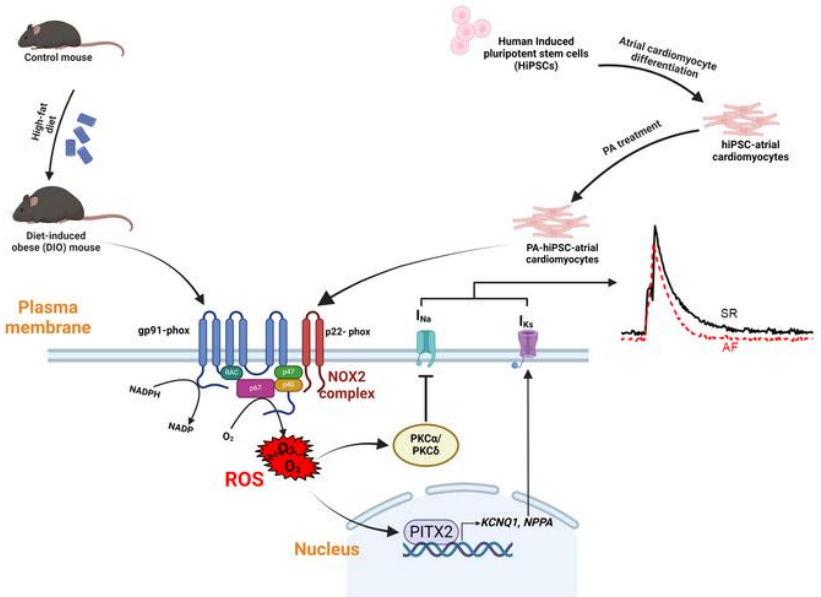

Find the latest version:

https://jci.me/175447/pdf

Modulation of NOX2 causes Obesity- Mediated Atrial Fibrillation

[1,2]Arvind Sridhar, [1]Jaime DeSantiago, [1]Hanna Chen, [1]Mahmud Arif Pavel, [1]Olivia Ly, [1]Asia Owais, [1]Miles Barney, [2]Jordan Jousma,[2] Sarath Babu Nukala, [3]Khaled Abdelhady, [3]Malek Massad,[3] Lorna Ernst Rizkallah, [1,2] Sang Ging Ong, [1,4]Jalees Rehman, [1,5]Dawood Darbar

[1]Division of Cardiology, University of Illinois-Chicago, Chicago, IL

[2]Department of Pharmacology, University of Illinois-Chicago, Chicago, IL

[3]Division of Cardiothoracic Surgery, University of Illinois-Chicago, Chicago, IL

[4]Department of Biochemistry and Molecular Genetics, University of Illinois-Chicago, Chicago, IL

[5]Department of Medicine, Jesse Brown Veterans Administration, Chicago, IL

[5]Correspondence

Corresponding author

Dawood Darbar, MD
Department of Medicine
Chicago, IL 60614
email: darbar@uic.edu

Conflict of interest: The authors have declared that no conflict of interest exists.

ABSTRACT

Obesity is linked to an increased risk of atrial fibrillation (AF) via increased oxidative stress. While NADPH oxidase II (NOX2), a major source of oxidative stress and reactive oxygen species (ROS) in the heart predisposes to AF, the underlying mechanisms remain unclear. Here, we studied NOX2-mediated ROS production in obesity-mediated AF using *Nox2*-knock-out (KO) mice and mature human induced pluripotent stem cell-derived atrial cardiomyocytes (hiPSC-aCMs). Diet-induced obesity (DIO) mice and hiPSC-aCMs treated with palmitic acid (PA) were infused with a NOX blocker (apocynin) and a NOX2-specific inhibitor, respectively. We showed that NOX2 inhibition normalized atrial action potential duration and abrogated obesity-mediated ion channel remodeling with reduced AF burden. Unbiased transcriptomics analysis revealed that NOX2 mediates atrial remodeling in obesity-mediated AF in DIO mice, PA-treated hiPSC-aCMs, and human atrial tissue from obese individuals by upregulation of paired-like homeodomain transcription factor 2 (PITX2). Furthermore, hiPSC-aCMs treated with hydrogen peroxide, a NOX2 surrogate, displayed increased PITX2 expression, establishing a mechanistic link between increased NOX2-mediated ROS production and modulation of PITX2. Our findings offer insights into possible mechanisms through which obesity triggers AF and support NOX2 inhibition as a potential novel prophylactic or adjunctive therapy for patients with obesity-mediated AF.

Keywords: atrial fibrillation, obesity, oxidative stress, NOX2, ROS, antioxidant therapy, PITX2

Introduction

Atrial fibrillation (AF), the most common sustained cardiac arrhythmia, is associated with an increased risk of stroke, heart failure, and death (1). Increasingly, population-based data has identified obesity (body mass index [BMI] ≥30 kg/m^2) as an independent risk factor for AF (2-4). Human and animal studies show that obesity-induced atrial remodeling creates a pro-fibrillatory substrate for AF (4-8). In diet-induced obese (DIO) mice fed a high fat diet (HFD), increased AF burden was seen to be mediated by both atrial structural and electrical remodeling (9). Importantly, the atria of DIO mice exhibited reduced cardiac sodium (I_{Na}) and calcium currents ($I_{Ca,L}$), while there was enhanced ultra-rapid delayed rectifier current (I_{Kur}) and increased fibrosis, leading to a shortening of the atrial action potential duration (APD) and reduced conduction velocity (CV) (9). However, the molecular mechanisms by which obesity mediates AF remain poorly understood.

Oxidative stress and the generation of reactive oxygen species (ROS) play a key role in mediating obesity-induced atrial remodeling and the development of AF (10).Increased lipolysis and the consequent increase in the exposure of myocardial tissue to fatty acids (FA) result in oxidative injury and inflammation in obese hearts (10-12). The primary sources of ROS production are NADPH oxidase (NOX), mitochondria, xanthine oxidase, cytochrome c oxidase, and nitric oxide synthase (13). Recently, NOX2 has emerged as a key player in the pathophysiology of AF with several findings linking the onset of AF to NOX2 upregulation (12-18). Studies have also shown that Nox2 upregulation drives angiotensin II-induced cardiac hypertrophy and fibrosis and ROS production (16). NOX2 is also a critical mediator of AF pathophysiology through its modulation of acetylcholine-activated inward-rectifying potassium current (I_{KACh}) via protein kinase C (PKC)-ε translocation to the cell membrane and NOX2 knockdown reduces the onset of AF in canines (16-18). In DIO mice, increased oxidative stress is specific to both mitochondria and cytoplasm and MitoTEMPO, a mitochondrial antioxidant, has been shown to reduce structural

remodeling and AF burden (9). However, the signaling pathways and mechanisms linking oxidative stress and atrial ion channel and structural remodeling remain unclear.

Most clinical trials using antioxidant therapy to treat AF have failed to show clinical benefit, in part because generic antioxidants such as vitamin C and MitoTEMPO target non-specific pathways of ROS production (20-21). Moreover, regardless of the source, ROS generates more ROS in the same way AF begets AF and facilitates the progression of AF from paroxysmal to persistent forms (10, 12-13). Thus, the identification and targeting of specific pathways involved in ROS production, such as NOX2, may not only prevent AF but also its progression in obesity-mediated AF.

Human induced pluripotent stem cell-derived atrial cardiomyocytes (hiPSC-aCMs) possess the complex array of ion channels that make up the atrial AP and closely mimic the electrical, structural, and metabolic features of human atrial tissue (HAT), thus, holding great promise for modeling AF (22-25). The most abundant FA found in obese individuals, palmitic acid (PA), increases the expression of NOX2 and the production of mitochondrial ROS in cardiomyocytes (10-12). This can lead to mitochondrial abnormalities and altered calcium homeostasis, and contribute to the development of AF in obesity (12). Thus, treating hiPSC-aCMs with PA creates an extracellular milieu that resembles obese human atria.

Altered expression of the paired-like homeodomain transcription factor 2 (PITX2), which has been associated with the chromosome 4q25 locus in AF patients, results in abnormal atrial electrical properties in both humans and mice, highlighting its significance in the pathophysiology of AF (26). Investigating the pro-arrhythmic effects of *PITX2*-induced electrical remodeling is a crucial step towards understanding and treating AF (26-27). However, the specific role of *PITX2* in obesity-mediated AF and increase in NOX2 remains unclear. Considering the link between NOX2 and atrial remodeling, we hypothesized that NOX2 drives oxidative stress and ROS, resulting in atrial channel and structure changes via modulation of PITX2 in obesity-mediated AF(15-19). To test this, we used a *Nox2*-knock-out mouse model and PA-treated hiPSC-aCMs

treated with apocynin (NOX blocker) (28-29) and GSK-2795039 (NOX2 inhibitor) (30). Collectively, both genetic and pharmacological inhibition of NOX2 in obese mice and PA-treated hiPSC-aCMs abrogate ion channel and structural remodeling and prevent obesity-mediated AF in part by transcriptional regulation of *PITX2*.

RESULTS

NOX2 is increased in atrial tissue of obese individuals: As NOX2 protein is increased in obesity-mediated AF in DIO mice,[9] we examined NOX2 levels in human atrial tissue of obese individuals with real-time qPCR. Individuals were grouped into lean (BMI 18.5 to 25 kg/m^2), overweight (BMI 25 to <30 kg/m^2), and obese (BMI >30.0 kg/m^2). BMI was the only key differentiator that was significantly changed in the overweight and obese groups compared to lean. Notably, other clinical parameters such as age, ejection fraction, left atrial size, and prevalence of conditions like diabetes mellitus, hypertension, coronary artery disease, and congestive heart failure did not exhibit statistically differences across the groups (Supplementary **Table S1**). We observed increased mRNA expression of human atrial *NOX2* in individuals with BMI>30 kg/m^2 (**Figure 1A**). While there was no significant change in *NOX2* expression among overweight individuals, obese individuals displayed more than a two-fold increase in atrial *NOX2* expression as compared with lean individuals (**Figure 1B**).

We then evaluated the expression of cardiac ion channels and structural genes. Though not statistically significant, obese individuals displayed a marked increase in the mRNA expression of *KCNA5* compared to lean individuals (**Supplementary Figure 1A**). Overweight and obese individuals also displayed a decrease in the mRNA expression of *GJA5*, which encodes connexin-40 of which the decrease in overweight patients was statistically significant (**Supplementary Figure 1B**). In contrast, *SCN5A* encoding I_{Na} was not significantly changed compared to lean individuals. (**Supplementary Figure 1C**) *CACNA1C* encoding $I_{Ca,L}$ showed a markedncrease in obese individuals as compared to lean individuals (**Supplementary Figure 1D**).

NOX2 inhibition prevents obesity-mediated AF: Given the association between NOX2 and atrial ion channel remodeling in obesity-mediated human AF, we investigated whether genetic knock out of NOX2 or pharmacological inhibition would reduce AF burden in an animal model of obesity (diet-induced obesity or DIO). We fed control (C57BL6J, DIO) and *Nox2*-KO male mice a 60% HFD for 10 weeks. Female mice were omitted from the study due to their heightened resistance to the obesogenic effects of HFD. Only obese mice that weighed >33g were included in the study. Some DIO mice were given a pharmacological NOX2 inhibitor, apocynin, in the drinking water (2 mg/mL; DIO-Apocynin).[28-29] We then assessed AF incidence and burden using transesophageal atrial burst pacing as we previously described.[9] DIO, DIO *Nox2*-KO, and DIO-Apocynin mice increased their weight compared to lean controls and *Nox2*-KO mice fed with the control diet (**Figure 1C**). The average weights of DIO, DIO-Apocynin, and DIO *Nox2*-KO mice were substantially increased compared to control, and *Nox2*-KO mice (39.6 ± 6.1g, 43.4 ± 8.1g, and 40.2 ± 4.8g respectively vs 31.7 ± 1.2g, and 24.9 ± 2.2g respectively) (**Figure 1D**). In our study, following transesophageal (TE) atrial pacing, we observed that both DIO *Nox2*-KO and DIO-Apocynin mice had a marked reduced AF burden compared to DIO mice. DIO *Nox2*-KO mice and DIO-Apocynin mice had 17.4 ± 31.8s and 28.3 ± 25.4s of AF compared to 167.3 ± 168.9s in DIO mice respectively (**Figure 1E-F**). Compared to the DIO mice, DIO *Nox2*-KO mice showed a significant reduction in AF incidence (% of mice that displayed AF/ total number of mice) compared to DIO-Apocynin mice (**Supplementary Figure 1E**). Collectively, our data shows that both genetic and pharmacological inhibition of NOX2 expression prevents pacing-induced AF in DIO mice.

Genetic suppression of Nox2 reverses obesity-mediated AF by normalizing atrial APD: To assess electrophysiologic (EP) impact of Nox2 deletion, we employed whole-cell cell patch clamping in freshly isolated atrial cardiomyocytes pooled from both LA and RA from control, DIO, *Nox2*-KO, and DIO *Nox2*-KO mice. First, DIO *Nox2*-KO mice displayed a prolonged atrial AP compared to DIO mice with substantial normalization of the APD20, APD50, and APD90

(*P*<0.05; **Figure 2A-B**, **Supplementary Figure 2A-B**). Second, both AP amplitude (APA_{max}) and the upstroke velocity (dV/dT_{max}) were significantly increased in DIO *Nox2*-KO mice compared to DIO mice (*P*<0.05; **Figure 2C**, **Supplementary Figure 2B**). Third, the atrial AP of DIO *Nox2*-KO mice closely resembled that of control and *Nox2*-KO mice and there were no changes in the APD20, APD50, APD90, APA_{max}, and dV/dT_{max} between the three groups (**Figure 2A-D**, **Supplementary Figure 2A, B, D)**. There were no changes to the resting membrane potential (RMP) across the four groups of mice (**Supplementary Figure 2C**).

DIO Nox2-KO mice restore APD by modulating I_{Na} and I_{ks}: Inducible AF in obese mice is mediated in part by ion channel remodeling of both I_{Na} and I_{Ks} (9). To determine if NOX2 protein inhibition restores atrial I_{Na}, we performed whole-cell voltage patch clamping in all four groups of mice. DIO *Nox2*-KO mice showed a significant increase in peak I_{Na} density when compared to DIO mice (**Supplementary Figure S3A–C**) with the restoration of I_{Na} densities at all test potentials similar to control and *Nox2*-KO mice (**Figure 2E-F**). There was also increased protein expression of Nav1.5 in DIO *Nox2*-KO and DIO-Apocynin mice compared to DIO mice (**Supplementary Figure 3D-F**). Nox2 increase leads to increased protein levels of PKC isoforms (31-32). Increased PKC-δ activity reduces overall $Na_V1.5$ expression and decreases I_{Na} (31-32). We performed Western blots on control, DIO, *Nox2*-KO, and DIO-*Nox2*-KO mice and showed that knockout of Nox2 reversed the obesity-induced increased protein level expression of PKC-α and PKC- δ isoforms (**Supplementary Figure 3G-H**)

Voltage clamping studies revealed that increased total I_K in DIO mice is reduced significantly in DIO *Nox2*-KO mice (**Supplementary Figure 4A**). Using HMR-1556 to quantify I_{Ks} indicated that NOX2 inhibition abrogates obesity-induced I_{Ks} in DIO *Nox2*-KO (**Figure 2I**). I_{Ks} densities at 30 mV and 50 mV were substantially reduced in DIO *Nox2*-KO mice versus DIO mice (**Figure 2I-J**). We then evaluated the mRNA and protein levels of several genes encoding the α- and β-subunits of the potassium channels with roles in AP repolarization. DIO *Nox2*-KO mice displayed decreased Kv7.1 and MinK protein expression compared to DIO mice, however, Kv1.5, another

major potassium channel involved in AF, remained unchanged (**Supplementary Figure 4C-4E**). DIO *Nox2*-KO mice showed reduced mRNA expression of *Kcnq1* and *Kcne1* which encodes for I_{Ks} and *Kcna5* which encodes for I_{Kur} (**Supplementary Figure 4B**). Lastly, gene and protein expression of *Kcnj3,* encoding the inward rectifying potassium channel Kir3.1 and forms a part of the acetylcholine-activated potassium channel (I_{KACh}), is significantly reduced in DIO *Nox2*-KO mice as compared to DIO mice (**Supplementary Figure 4B, 4G**). We previously showed that increased atrial natriuretic peptide (ANP) activity modulates I_{Ks} in hiPSC-aCMs harboring an *NPPA* mutation (23, 33). mRNA expression and protein expression of ANP was markedly increased in DIO mice as compared to controls, but the increase was abrogated in DIO *Nox2*-KO mice (**Supplementary Figure 4B, 4G**).

NOX2 inhibition improves contractility in DIO mice and PA-hiPSC-aCMs: Reduction of the density of the $I_{Ca,L}$, which is generated by channels composed of Cav1.2 (encoded by *CACNA1C*), β2 (*CACNB2*), and α2δ (*CACNA2D*) subunits, is a hallmark of the atrial electrical remodeling in DIO mice (9). The reduction in $I_{Ca,L}$ induces a reduction in calcium release from the sarcoplasmic reticulum (SR) and reduced overall atrial contractility. To further evaluate this change, we used voltage clamping studies on pooled mouse atrial cardiomyocytes to measure $I_{Ca,L}$ along with calcium transient measurements using fluorescent calcium dye Fura-2 in DIO *Nox2*-KO mice **(Figure 2G-H, 3A-H)**. $I_{Ca,\,L}$ reduction in DIO mice was markedly reversed in DIO *Nox2*-KO mice **(Figure 2G-H)**. We also observed a reduction of intracellular Ca^{2+} ($[Ca^{2+}]_i$) in DIO atrial cells which was reversed in DIO *Nox2*-KO atrial cells, thus, highlighting an increased magnitude of calcium release from the SR in DIO *Nox2*-KO mice **(Figure 3E)**. DIO atrial cells also showed a substantial decrease in sarcomeric cell shortening, a measure of atrial contractility, compared to control and DIO *Nox2*-KO atrial cells **(Figure 3F).** There were no statistical differences in the time to peak and relaxation time between the four groups **(Figure 3C, D, G, H)**

NOX2 inhibition in PA-treated-hiPSC-aCMs using NOX2 small molecule inhibitor reverses obesity-induced ion channel remodeling: Retinoic acid (RA) was used specifically to induce

hIPSC-aCM differentiation from hiPSCs. Flow cytometry revealed a significant increase in the percentage of cells expressing Kv1.5 in RA-treated cells compared to dimethyl sulfoxide (DMSO)-treated cells whilst there was a decrease in the percentage of cells expressing MLC2v, a ventricular marker **(Supplementary Figure 11A-D)**. We used mature hiPSC-aCMs treated with PA and a NOX2 small molecule inhibitor, GSK-2795039 (20μM dissolved in DMSO, PA-GSK-hiPSC-aCMs), and oleic acid (OA, at 0.5 μM) for 5 days to study the effects of NOX2 in mediating FA-induced atrial remodeling. Optical voltage mapping experiments on PA-GSK-hiPSC-aCMs showed similar results to DIO *Nox2*-KO mice with a reversal in shortened AP in PA-GSK-hiPSC-aCMs compared to PA-hiPSC-aCMs at the 10,50, and 90% repolarization (**Figure 4A-D)**. Similar to DIO mice, hiPSC-aCMs treated with PA also display increased I_{Ks} and total I_K, which was reversed in PA-GSK-hiPSC-aCMs **(Figure 4E-F)**. Whole cell patch clamping studies revealed that chronic PA treatment shortened APD at 20, 50, and 90% repolarization whilst OA treatment markedly prolonged APD50 and increased the maximum upstroke velocity (**Supplementary Figure S7A-E**). PA-hiPSC-aCMs in contrast to Bovine Serum Albumin (BSA)-hiPSC-aCMs showed a marked reduction in the maximum upstroke velocity and maximum amplitude of the AP (APAmax) (**Supplementary Figure S7E-F**). Moreover, PA-hiPSC-aCMs also showed decreased I_{Na} and $I_{Ca,L}$ densities in control hiPSC-aCMs which was reversed in PA-GSK-hiPSC-aCMs **(Figure 4G-J)**. Thus, our results suggest that genetic deletion and pharmacological inhibition of NOX2 abrogates atrial APD shortening mediated by obesity and rescues obesity-induced AF in both DIO *Nox2*-KO mice and PA-GSK-hiPSC-aCMs.

Echocardiographic analyses show that DIO mice display increased LA size compared to control mice (**Supplementary Figure 5A, C; Supplementary Table S2**). While DIO mice showed both LA and right atrial (RA) enlargement compared to controls, only LA size was abrogated in DIO *Nox2*-KO mice (**Supplementary Figure 5C**). There was no notable difference in the right ventricular (RV) area between the 4 groups of mice. Other echocardiographic parameters such

as the left ventricular ejection fraction (LVEF), fractional shortening (FS), pulse wave ratio between active and passive ventricle filling (A'/E'), cardiac output (CO), LV posterior wall diameter (LVPW)

were unchanged across the 4 groups of mice (**Supplementary Figure 5B, D-E, Table S2**).

NOX2 inhibition prevents obesity-mediated atrial fibrosis and increases atrial CV: To study changes in conduction, epicardial multielectrode array (MEA) mapping of both atria and the left ventricle was performed in isolated Langendorff-perfused beating hearts from all four mouse groups. The CVs were reduced in both atria and the left ventricle in DIO, *Nox2*-KO, and DIO *Nox2*-KO mice compared to controls. However, DIO *Nox2*-KO mice showed improved left and right atrial and left ventricular CV compared to DIO mice (**Figure 5A-D**, **Supplementary Figure 6B-C**). The isochronal maps also illustrate a pattern consistent with improved CV in both atria of DIO *Nox2*-KO mice compared to DIO mice (**Figure 5A-D**). We then determined if NOX2 inhibition reduces obesity-induced atrial fibrosis by using picosirius red and Masson's trichrome staining on histological sections from control, DIO, and DIO-*Nox2*-KO mice. LA and RAsections from DIO mice showed increased fibrosis compared to both control and DIO *Nox2*-KO mice (**Figure 5E-H**). However, there were no differences in fibrosis in the ventricular slices of all four mouse groups (**Supplementary Figure 7A**).

Nox2 inhibition reduces ROS production in both DIO mice and PA-hiPSC-aCMs: Utilizing H2DCFDA staining, a well-established technique for both visualizing and quantifying cytosolic ROS (61, 63-65), we assessed ROS levels in control, DIO mice, *Nox2*-KO mice, DIO *Nox2*-KO atrial myocytes (pooled LA and RA cardiomyocytes) , and BSA, PA, and PA-GSK-hiPSC-aCMs (**Figure 6A-F**). Measurements were taken at baseline and after 12 minutes of staining. Substantial elevations in ROS levels were observed in DIO mice from baseline, distinct from control, *Nox2*-KO, and DIO *Nox2*-KO mice atrial myocytes. This increase continued progressively over 12 minutes; a trend exclusive to the DIO group (**Figure 6B-C**). Similarly, PA-treated hiPSC-aCMs

showed increased ROS levels from the start with a marked rise noted over the 12-minute period, compared to the BSA and PA-GSK-hiPSC-aCMs (**Figure 6E-F**).

Global proteomics and pathway enrichment analysis: To identify the potential pathways involved in obesity-mediated AF, we performed proteomic profiling of pooled LA and RA protein lysates from control, DIO, and DIO *Nox2*-KO mice using a Q Exactive HF mass spectrometer coupled with an UltiMate 3000 RSLC nanosystem with a Nanospray Frex Ion Source (Thermo Fisher Scientific). The total number of identified proteins across the three groups was 3370 proteins, of which primarily cardiac related genes were focused (**Supplementary Figure 8A-D**). Contractile proteins such as Myl3, Ace, TnnI2, and TnnI3k were seen to be downregulated in DIO atria in comparision to both control and DIO *Nox2*-KO mouse atria (**Supplementary Figure 8A-B**). In comparison, proteins involved in fatty acid metabolism such as Cpt1a, Fabp4, and Acsl5 were upregulated in DIO mouse atria compared to control and DIO *Nox2*-KO mouse atria (**Supplementary Figure 8A-B**). The number of differentially regulated proteins (log 2-fold change ± 0.5) in the DIO versus control comparison were 41 of which 33 were upregulated and 8 downregulated (**Supplementary Figure 8C**). In the DIO-*Nox2*-KO mice compared to DIO mice, 7 were upregulated and 48 downregulated (**Supplementary Figure 8D**).

To identify the signaling pathways that modulate Nox2-mediated atrial remodeling in DIO and DIO-*Nox2*-KO mice, we used Kyoto Encyclopedia of Genes and Genomes (KEGG) pathway enrichment analysis. Major common downregulated pathways that were enriched in both the DIO versus control and DIO versus DIO-*Nox2*-KO mice included the cardiac muscle contraction pathway (hsa04260), the dilated cardiomyopathy pathway (hsa05414), and the hypertrophic cardiomyopathy pathway (hsa05410) (**Supplementary Figure 8E-F**). In contrast, pathways that regulate increased FA metabolism and FA digestion and absorption were the commonly implicated upregulated pathways (**Supplementary Figure 8G-H**). In total, 22 pathways were commonly downregulated, and 6 pathways were upregulated (**Supplementary Figure 8I-J**). We further validated three major pathways with Western blot: cardiac muscle contraction pathway

(hsa04260), FA metabolism pathway (hsa0061), and oxidative phosphorylation pathway (hsa00190) (**Supplementary Figure 8E-H**). This revealed that proteins modulating the cardiac muscle contraction pathway such as cTnI, cTnT, Mybpc3, Mymo1, and Mlc2v are ubiquitously decreased in DIO mice and their expression levels are restored in DIO-*Nox2*-KO mice (**Supplementary Figure 9A-D, F**). Only Myl7 decrease wasn't reversed after NOX2 inhibition (**Supplementary Figure 9E**). Expression of proteins involved in FA metabolism such as Cpt1α, Pparα, and Fabp3 were abrogated in DIO-*Nox2*-KO mice, which was increased in the DIO mice (**Supplementary Figure 10A-C**).

Transcriptomic and gene regulatory network analysis on HAT and hiPSC-aCMS. HAT from obese individuals showed increased *NOX2* mRNA expression along with increased KCNA5 and decreased GJA5 mRNA expression compared to lean individual HAT (**Figure 1A-B, Supplementary Figure 1A-B**). We then performed an unbiased global transcriptomic analysis by RNA sequencing (RNA-Seq) separately on lean vs obese HAT, control hiPSC-aCMs versus PA-hiPSC-aCMs, and PA-hiPSC-aCMs versus PA-GSK-hiPSC-aCMs to compare the differentially regulated gene expression pathways (**Figure 7A-D**). Pathway enrichment analysis showed that the three comparisons shared 5 KEGG pathways **(Supplementary Figure 10A)**, 21 gene ontology (GO) molecular function pathways **(Supplementary Figure 10C)**, and 32 GO biological process pathways **(Supplementary Figure 10E)**. Cardiac-related GO biological process pathways commonly enriched between the three comparisons were 1) Cellular response to oxygen-containing compound (GO1901701), 2) Cardiac muscle tissue development (GO0048738), 3) Regulation of heart contraction (GO0008016), 4) Potassium ion transport (GO0006813), and 5) Potassium ion transmembrane transport (GO0071805) (**Figure 7A**). Potassium ion transmembrane transport (GO0071805), a pathway consisting of major potassium channels involved in AF was specifically studied in all three comparisons. (**Figure 7B-D**) Common cardiac-related KEGG pathways between the three comparisons were 1) PPAR

signaling pathway (hsa03320) (**Supplementary Figure 10I-J)**, 2) MAPK signaling pathway (hsa04010), 3) Calcium signaling pathway (hsa04020) (**Supplementary Figure 10F-H)**, 4) Hypertrophic cardiomyopathy pathway (hsa05410) and 5) Dilated cardiomyopathy pathway (hsa05414) (**Supplementary Figure 10B**). Common cardiac GO molecular function pathways were 1) Calcium ion binding (GO0005509), 2) Potassium channel activity (GO005267), 3) Voltage-gated potassium channel activity (GO005249), and 4) Voltage-gated cation channel activity (GO022843) (**Supplementary Figure 10D**). Of the common KEGG and GO pathways, we selected the Potassium ion transport, Potassium ion transmembrane transport, voltage-gated potassium channel activity, lipid localization Gene Ontology Term (GO0010876), and voltage-gated cation channel activity to perform upstream regulator analysis to identify potentially novel independent and integrated transcription factor (TF) networks and upstream TFs that might regulate the above key pathways (**Figure 7E)**. Common TFs that are upregulated in all the RNAseq comparisons were – *PPARA, PITX2*, *ESRRA, TBX5, GATA4,* and *TCF12*. Common TFs that were downregulated in all the RNA-Seq comparisons are – *FOSL1, TCF21*, *FOXM1, FOXE1*, and *KLF4*. qPCR validation of both HATs and hiPSC-aCMs showed that *PITX2,* and *TBX5* were increased in obese HATs and PA-hiPSC-aCMs (**Figure 7F-G**). Similarly, DIO *Nox2*-KO mice showed reduced protein expression of *PITX2* suggesting that NOX2 inhibition prevents obesity-induced atrial remodeling through *PITX2* (**Figure 7H-I**). Lastly, to investigate if NOX2 increase is associated with increased mRNA *PITX2* expression, we treated BSA-hiPSC-aCMs with 25 μM of hydrogen peroxide (H_2O_2) for 5 days. H_2O_2-hiPSC-aCMs showed a similar increase in *PITX2* mRNA expression compared to PA-hiPSC-aCMs, thus suggesting that PITX2 is indeed upregulated by ROS (**Figure 7J**).

To directly assess the role of PITX2 in obesity-mediated ion channel remodeling, we performed small interfering (si) RNA knockdown (KD) experiments in PA-hiPSC-aCMs (**Figure 8**). hiPSC-aCMs transfected with *PITX2* specific siRNA and treated with both BSA and PA showed ≈ 40% decrease in *PITX2* expression compared to HiPSC-aCMs transfected with a scrambled

sequence (**Figure 8A**). *PITX2* KD markedly abrogated PA-induced EP changes, including reversing the shortening of atrial APD20, APD50 and APD 90 (**Figure 8C-E**), decrease in maximum upstroke velocity (**Figure 8F**), and maximum action potential amplitude (**Figure 8G**), compared to PA-Scrambled-hiPSC-aCMs. Our results provide strong evidence that increase in PITX2 directly modulates EP changes in obesity-mediated AF.

Discussion

Oxidative stress plays a key role in mediating obesity-induced AF by the activation of NOX2, a major non-mitochondrial source of ROS production (11-13). Antioxidants, however, have not shown any benefit for treating AF, in part because of their failure to target the specific pathways of ROS production (20-21). Here, using both *Nox2*-KO mice and mature hiPSC-aCMs, we showed that NOX2 mediates increased oxidative stress and ROS production in obesity-mediated AF. Treatment of DIO and DIO-*Nox2*-KO mice with generic NOX blocker, apocynin and PA-treated hiPSC-aCMs with a NOX2-specific inhibitor, GSK2795039 abrogated obesity-mediated ion channel remodeling and atrial fibrosis by reducing oxidative stress and ROS production. Unbiased transcriptomics and gene regulatory network analysis revealed that NOX2 mediates atrial ion channel and structural remodeling in obesity-mediated AF in DIO mice, PA-treated hiPSC-aCMs, and human atrial tissue from obese individuals by the upregulation of PITX2. Treatment of hiPSC-aCMs with hydrogen peroxide, a known by-product of NOX2 increased *PITX2* mRNA expression, suggesting ROS-mediated upregulation of PITX2 in obesity-mediated AF. Collectively, our findings show that genetic and pharmacological inhibition of NOX2 abrogates ion channel and structural remodeling in both *Nox2*-KO mice and in mature hiPSC-aCMs and prevents the development of obesity-mediated AF by modulating PITX2 expression.

Oxidative stress and ROS production mediate myocardial remodeling through the creation of an electrophysiologic (EP) substrate for arrhythmogenesis (18-19). The assessment of atrial EP of DIO-Apocynin, DIO-*Nox2*-KO mice, and PA-GSK-hiPSC-aCMs showed prolongation of atrial APD, normalization of remodeled ion channels, a decrease in atrial fibrosis, and an increase in

atrial CV as compared with the DIO mice. We previously reported that DIO mice are more prone to AF by upregulating the Kv1.5 and I_{Kur} along with downregulation of Nav1.5 and I_{Na}, causing shortening of the atrial APD (9). In humans, loss-of-function *SCN5A* mutations, encoding Nav1.5, not only decrease cardiac conduction and shorten atrial APD, but also increase susceptibility to AF (34-35). Thus, improvements in both atrial APD and CV and restoration of I_{Na} in DIO *Nox2*-KO mice support reduced AF vulnerability in these mice. Studies have reported that both cytosolic and mitochondrial ROS downregulate Nav1.5 via PKC-dependent phosphorylation of the channel (12, 31-32). Secondly, chronic treatment of AngII, a mediator of NOX2 increase has been seen to directly significantly reduce INa at 10 days and 21 days (36). Thus, our data that showed failure to increase PKC-α and PKC-δ expression in DIO *Nox2*-KO mice as compared to DIO mice provides a plausible explanation for the modulation of I_{Na}.

We previously reported that DIO mice are more susceptible to AF due to ion channel remodeling, causing shortening of the atrial APD (9). Here, we showed that cardiac muscle contraction, potassium transmembrane transport, and PPAR signaling were enriched in the proteomics analysis of control, DIO, and DIO-*Nox2*-KO mice and the RNA-Seq analysis of BSA, PA, PA-GSK-hiPSC-aCMs, and obese HAT. Upstream regulator analysis identified *PITX2* as a major upregulated gene in obese HATs, and PA-treated hiPSC-aCMs compared to lean HATs and BSA and PA-GSK-hiPSC-aCMs, respectively. While, there have been extensive research on the impact of loss-of-function *PITX2* in atrial arrhythmogenesis (26-27), the role of increased *PITX2* in atrial remodeling is unclear. First, measuring *PITX2* expression in human atrial myocytes from patients in sinus rhythm and AF, Perez-Hernandez et al. found that increased I_{Ks} and reduced $I_{Ca,L}$ was mediated by increased *PITX2* expression implicating its role in electrical remodeling during AF (37-38). Second, treating BSA-hiPSC-aCMs with H_2O_2, which has been shown to increase NOX2-mediated ROS production (39), increased *PITX2* as seen with PA treatment. Importantly, studies have shown that H_2O_2 incubation in ventricular myocytes leads to decreased cardiac I_{Na} density (13). In addition, PITX2 KD using siRNA abrogated the EP effects of PA

385 treatment in PA-hiPSC-aCMs compared to PA-treated-Scrambled-hiPSC-aCMs. Collectively, our
386 findings suggest that increased NOX2 is associated with *PITX2* upregulation, which mediates ion
387 channel remodeling in obesity-mediated AF. Nonetheless, additional studies will be necessary to
388 fully elucidate this link in both in-vivo and in-vitro models.

389 A major determinant of altered atrial APD is potassium channel activity (40). Mutations in
390 *KCNQ1*, *KCNA5*, and *KCNH2* encoding I_{Ks}, I_{Kur}, and I_{Kr} respectively have been implicated in the
391 pathogenesis of early-onset AF (40-42). DIO-*Nox2*-KO mice showed a marked reduction in total
392 I_K and I_{Ks}, and reduced mRNA expression of *KCNQ1* and *KCNE1*, which encode I_{Ks}. The
393 normalization of I_{Ks} in DIO-*Nox2*-KO mice and PA-GSK-hiPSC-aCMs as compared to DIO mice
394 and PA-treated hiPSC-aCMs respectively is in part explained by the oxidation of potassium
395 channels, especially Kv7.1 (36). We and others have shown that gain-of-function mutations in
396 *NPPA*, encoding ANP, have also been associated with increased I_{Ks} (25, 43-44). We recently
397 reported that increased I_{Ks} expression and function were accompanied by atrial AP shortening in
398 hiPSC-aCMs expressing an *NPPA* mutation in hiPSC-aCMs (23). Secondly, ANP expression
399 intrinsically mediates electrical remodeling and cardiac electrophysiology through cAMP signaling
400 as evidenced by previous studies (43-44). ANP and NOX generation have also been linked
401 through a feed-forward cycle via the NOX/Src axis, promoting excess production of both
402 (45).Importantly, *NPPA* mRNA expression is increased in DIO mice but is unchanged in DIO-
403 *Nox2*-KO mice. Thus, we postulate that enhanced I_{Ks} is due to increased NOX2 expression
404 directly modulating increased ANP secretion in DIO mice.

405 We applied an electro-metabolic maturation approach to generate mature hiPSC-aCMs that
406 are the best available surrogate for atrial tissue (22-25). Our findings demonstrate that blocking
407 NOX2 effectively prevents obesity-mediated ion channel remodeling and atrial fibrosis by
408 reducing oxidative stress and ROS production in both DIO mice and PA-treated hiPSC-aCMs.
409 Furthermore, to model obesity in-vitro and recapitulate increased oxidative stress and lipid
410 overload, mature hiPSC-aCMs were chronically treated with PA, the most common FA in the

411 human diet, to increase serum-free FA circulation in the heart (46-48). Studies on PA treated
412 murine cardiomyocytes and HL-1 cells showed that PA alone selectively increases NOX2
413 expression, mitochondrial abnormalities, aberrant calcium transients, and arrhythmia as
414 compared to OA (14).Our findings also revealed a distinct response to OA treatment,
415 characterized by a prolongation of atrial AP with increase in the APD50 and the maximum
416 upstroke velocity in contrast to PA treatment. Importantly, the differential effects observed
417 between OA and PA treatments suggest that the abnormalities in obesity-related cardiac
418 dysfunction are mostly driven by saturated fats like PA.

419 We used a global *Nox2*-KO mouse model to examine the role of NOX2 in obesity-mediated
420 AF. As NOX2 is expressed not only in cardiomyocytes and endothelial cells but also in fibroblasts,
421 and inflammatory cells, it is possible that other cell types may contribute to the adverse atrial
422 remodeling (49). Studies have also shown previously that an increase in ROS in DIO hearts is
423 primarily generated by an increase in NOX2 rather than mitochondrial specific NOX4 (52).
424 Interestingly, a recent report showed that superoxides can directly activate mitochondrial K_{ATP}
425 channels, which may explain the effectiveness of generic mitochondrial ROS scavengers such as
426 mitoTEMPO in reversing the atrial phenotype in obese mice (53-54). Furthermore, H2DCFDA
427 staining in both rescue groups, DIO Nox2-KO mice and PA-GSK-hiPSC-aCMs showed reduced
428 ROS compared to the obese groups, DIO mice and PA-hiPSC-aCMs which suggests that ROS
429 production in the atria of DIO mice and PA-hiPSC-aCMs are driven by increased NOX2
430 expression.

431 NOX2-derived ROS and changes in intracellular redox state lead to aberrant calcium release
432 and arrhythmias by modulating excitation-contraction coupling through oxidative modifications of
433 ryanodine receptor 2 (RyR2), CamKII, phospholamban, and sarco/endoplasmic reticulum
434 calcium-ATPase (SERCA2a) (55-56). For example, oxidative activation of CaMKII through ROS
435 signaling has been shown to be pro-arrhythmic in diabetic mice and is linked to the pathogenesis
436 of several cardiac diseases including AF (57-58). Our proteomics analysis suggests that cardiac

muscle contraction was markedly reduced in DIO mice but restored in DIO-*Nox2*-KO mice. DIO mice also exhibited reduced $I_{Ca,L}$ and atrial contractility, which was reversed in DIO-*Nox2*-KO mice. Given the important relationship between NOX2 and redox-mediated changes to excitation-contraction, a combined strategy targeting both calcium handling proteins and NOX2 should be a focus for future studies. Our data suggests that the reduction in the Cai amplitude is more reflective of the reduction in the $I_{Ca,L}$ (Figure 2G-H) which decreases the excitation contraction coupling gain and not due to changes in RyR2 that could affect the sarcoplasmic reticulum Ca release. We also showed that NOX2 protein inhibition prevents obesity-induced LA enlargement in DIO-*Nox2*-KO mice. As NOX2 has been implicated in cardiac hypertrophy (17-21), our data suggest that NOX2 inhibition may be a viable therapeutic approach for atrial hypertrophy.

Our studies emphasize the key role played by NOX2-generated ROS and PITX2 in obesity-mediated AF. Our mechanistic studies demonstrate that targeting atrial oxidative injury and ROS production with both a NOX blocker and a NOX2-specific inhibitor and genetic ablation of NOX2 in obese mice and PA-treated hiPSC-aCMs may not only prevent and treat AF but also slow its progression in obese individuals. Our findings have important implications for targeted therapy for AF patients with obesity. As the response to current antiarrhythmic drugs in an individual patient is highly variable and membrane-active drugs can be associated with significant toxicity, targeted inhibition of NOX2 may be a novel therapeutic approach for obese individuals at risk for AF and as adjunctive therapy for patients with obesity-mediated AF.

Limitations

First, we utilized both left atrial and right atrial samples for whole-cell patch clamping, EP, and molecular analysis. However, it is essential to acknowledge that the right and left atria are known to exhibit significant differences in gene expression and function. These intrinsic disparities could impact our findings and should be carefully considered when interpreting the results. This limitation underscores the importance of analyzing both atria separately to fully understand the distinct electrophysiological and molecular characteristics of each chamber in the context of our

study. Second, using mature hiPSC-aCMs treated with FAs as an experimental model, though valuable, represents a simplified approach and thus cannot recapitulate the in vivo complexity of obesity, which consists of many lipids. Second, it has been established that current protocols do not achieve fully differentiated atrial cardiomyocytes and result in some heterogeneity. Our protocol typically yields ~80 to 90% pure iPSC-aCMs and <6% fibroblasts based on immunostaining analysis as we have previously described and show in **Supplementary Figure S11** (23-25). Third, GAPDH and β-actin were utilized as housekeeping genes for qPCR and western blotting analyses. Reports indicate that the expression levels of GAPDH and β-actin can be affected in the LV and RA of hearts from aged and diabetic models, with these alterations being chamber-specific (66-67). Despite this, some findings suggest that GAPDH possesses high expression stability in heart failure and normal heart conditions (67). Nonetheless, a broader range of housekeeping genes may further strengthen our findings.

METHODS

Sex as a Biological Variant

In this study, only male mice were used because female mice do not reach the 33g obesity threshold after ten weeks on a high-fat diet (HFD), due to their resistance to obesogenic effects (9). Control C57BL6J and Nox2-KO male mice were fed a 60% HFD from Teklad (#TD06414) for ten weeks (9). For experiments involving human atrial tissue, samples were from both males and females. However, sex as a biological variable was not considered due to insufficient statistical power to analyze sex-stratified effects. Further research is needed to determine whether these findings apply to females and to understand sex-specific differences in obesity-mediated atrial fibrillation.

Human Atrial Tissue

We obtained written informed consent to collect adult human atrial tissue during cardiothoracic surgery under a University of Illinois Chicago Institutional Review Board-approved protocol. The

atrial tissue was obtained, stored, and processed as we previously described (23). Briefly summarizing, we obtained atrial tissue from the right and left atrium at the time of surgery during venous cannulation after which it was transported to the lab in warmed EDTA as previously described (69). Half the tissue was used for aCM isolation using a Langendorff-free isolation protocol[69] and the other half was immediately snap frozen using liquid nitrogen for further use for RNA and protein isolation (23). For RNA extraction, 0.5 mL of TRIzol was added to the sectioned tissue and was stored at -80ºC.

Mouse models generation

Animal studies were conducted following approved protocols by the University of Illinois at Chicago's institutional animal care and use committee (ACC) and adhering to NIH guidelines. The study utilized *Nox2*-KO mice (gp91phox-/- or Cybb-/-) with a neomycin resistance gene inserted at exon3 of gp91phox, resulting in the absence of NOX2 heterodimer complexes and subsequent lack of superoxide production (59). Breeding experiments involved male hemizygous mice crossed with control C57BL/6J mice and *Nox2*-KO mice.

DIO mice generation

Control C57BL6J and *Nox2*-KO mice were fed a 60% HFD from Teklad (#TD06414) for ten weeks as we previously described (9). We previously reported that female mice don't reach the 33g threshold for obesity after ten weeks. Thus, only male mice participated in the study.

Human iPSC culture and hiPSC-aCM differentiation

HiPSC-aCMs were generated from reprogrammed peripheral blood mononuclear cells (PBMCs) from patient 1 (P1), with no prior diagnosis of AF recruited to the Human Cardiac Atrial Tissue Biorepository as previously described (23). hiPSCs were seeded at 500,000 cells/well on vitronectin-coated plates and cultured in mTesR media until 80-90% confluent. Differentiation was initiated using the Cardiomyocyte Differentiation Kit (Gibco) and guided toward the atrial subtype using all-trans retinoic acid (22-25). The cellular population was purified through glucose starvation and lactate replacement, resulting in contracting monolayers. Our protocol typically

yields ~80 to 90% pure iPSC-aCMs and <6% fibroblasts based on immunostaining analysis as we have previously described (23-25) and show in **Supplementary Figure S11**. iPSC-aCMs were then matured following dissociation and replating on fibronectin-coated plates and maintained in Cardiomyocyte Maintenance Media supplemented with T3, insulin-like growth factor-1, dexamethasone, and bovine serum albumin (BSA)-bound PA/OA as previously described (22-25).

Fatty acid treatment and Nox2 inhibition in hiPSC-aCMs

To prepare PA and OA solutions, approximately 1 ml of 250mM FA solutions were made in 100% molecular grade ethanol. PA, being a powder and OA, being liquid at room temperature, were measured out into Eppendorf tubes under sterile conditions. The saturated FAs in ethanol were then placed in a 70°C water bath until they dissolved, and the solution became clear, a step necessary due to their insolubility at room temperature. For a 7:1 FA mixture of 25mL, 1.061mL of the solution was used, adding 265.3uL of each FA to achieve the target FA stock concentration of 10.5uM. The stock concentration was in turn dissolved in cardiomyocyte maintenance media to get a final FA concentration of 500uM. Mature hiPSC-aCMs were exposed to either BSA or BSA-conjugated PA or OA at a concentration of 500μM each for 5 days to mimic FA exposure observed in obesity. In the case of PA-GSK-hiPSC-aCMs, GSK2795039 was resuspended in DMSO and dissolved in PA-conjugated media to achieve a final concentration of 20 μM. Similar to PA-hiPSC-aCMs, PA-GSK-hiPSC-aCMs were treated with this media for 5 days.

Cellular electrophysiology, calcium transient recordings, and electrical mapping studies.

Left and right atrial cardiomyocytes from mice were isolated in a Langendorff perfusion system, as previously described. Whole-cell patch clamping on both mouse cardiomyocytes and hiPSC-aCMs for APD, I_{Na}, $I_{Ca,L}$, and I_{Ks} recordings was performed according to previously published protocols (9, 60-61). Optical voltage mapping recordings were performed on the IonOptix system myopacer system using the fluovolt membrane potential kit (Thermo Fisher). HiPSC-aCMs attached to confocal dishes were incubated with Tyrode's solution (140 mM NaCl, 4.56 mM KCl,

0.73 mM $MgCl_2$, 10 mM HEPES, 5.0 mM dextrose, 1.25 mM $CaCl_2$) containing 1x Fluovolt (Sigma/Aldrich) for 15-20 minutes. Cells were then washed with normal Tyrode's solution before being viewed on the eGFP setting for APD recordings (23).

For calcium transients, isolated LA and RA cardiomyocytes were plated on laminin-coated coverslips and observed under an inverted Nikon TE300 microscope. The cells were incubated with 2 μM Fura-2 AM for 15 minutes, followed by a washout period of 20 minutes for dye de-esterification. Excitation was performed at 340 and 380 nm, and emission was detected at 510 nm. Transillumination with red light (>650 nm) was used to avoid interference with fura-2 epifluorescence. Contractility was measured by tracing sarcomere length. Field stimulation was applied at 1 Hz until a steady state was reached, and contractility and [Ca2+]i transients (amplitude and kinetics) were analyzed using IonOptix software (61).

Isolated Langendorff-perfused hearts underwent left and right atrial and ventricular epicardial activation mapping (61). Using previously published protocols that used Mapping Labs electrical mapping system, a 2-dimensional multielectrode array (MEA) containing 64 electrodes in a 8x8 grid was used to study activation times and atrial and ventricular conduction velocities computed at a cycle time of 100 ms (62) . The propagation of the beats across the left atrium (LA), right atrium (RA), and left ventricle (LV) over 5 seconds were analyzed. Activation maps were generated for each beat, depicting sequential activation from one localized region to the entire matrix area. CV was determined by measuring the time required for propagation from the point of minimum to maximum activation. The averaged conduction velocity is computed and binned where each bin contains enough vectors that have similar directions. This process was repeated across beats from different recordings for a specific sample and the overall average CV for each sample was calculated from these measurements.

Atrial fibrosis measurements

Preparation of paraffin sections and subsequent staining was done using the services of the Research Histology Core at the University of Illinois Chicago. For atrial fibrosis analysis, we

followed previously published protocols (9). We harvested and fixed mouse hearts in 10% neutral formalin overnight, embedded them in paraffin, and cut 5 μm thick sections using the Microm HM340E at the histology core. These sections were stained with Masson's trichrome and picosirius red stains (Sigma) after de-paraffination. The cardiac fibrosis ratio was analyzed and calculated using Image J by dividing the total cardiomyocyte area in the atrium.

qPCR analyses

Total RNA was isolated from human atrial tissue, mouse LA and RA, and hiPSC-aCMs using TRIzol reagent (Invitrogen), following the manufacturer's instructions to ensure the extraction of high-quality RNA. The concentration and purity of the isolated RNA were meticulously assessed using a NanoDrop 2000 spectrophotometer (Thermo Fisher Scientific), with 1 μg of total RNA utilized for each reverse transcription reaction. Reverse transcription to synthesize cDNA was conducted using SuperScript III Reverse Transcriptase (Thermo Fisher Scientific), adhering to the manufacturer's protocol to optimize the fidelity and efficiency of the cDNA synthesis.

For the quantitative polymerase chain reaction (qPCR) analysis, specific assays and primers were selected for target genes (detailed in **Supplementary Table S2**) with glyceraldehyde 3-phosphate dehydrogenase (GAPDH) serving as the normalization reference gene. qPCR reactions were performed on an ABI QuantStudio 5 system (Applied Biosystems), using SYBR Green PCR Master Mix to accurately detect and quantify PCR amplification products. The thermal cycling conditions were carefully optimized specific to each target assay, comprising an initial denaturation step followed by 40 cycles of denaturation, annealing, and extension. Relative expression levels of the target genes were calculated employing the ΔΔCt method, by the quantification of gene expression changes in the experimental samples relative to control. For the Δ*CT* Calculation**,** the cycling time (CT) value of the target gene was subtracted from the CT value of GAPDH in the same sample using $\Delta CT = CT_{\text{target gene}} - CT_{\text{reference gene}}$. The ΔΔCT value was then calculated using $\Delta\Delta CT = \Delta CT_{Experimental} - \Delta CT_{Control}$. The relative expression for the gene was in turn calculated using Relative gene expression= $2^{-\Delta\Delta CT}$.

Protein isolation and Western blots

Proteins from both mouse hearts and HiPSC-aCMs were isolated based on previously published protocols using 1X RIPA buffer (9,23). Each sample containing 50 µg of protein was subjected to SDS-PAGE gel electrophoresis. The resolved gels were then electro-transferred onto 0.2 µm PVDF membranes. Following a 2-hour blocking step with 5% BSA, membranes were probed with specific antibodies for target proteins **(Supplementary Table S3)**. Blots were developed using either anti-rabbit HRP or anti-mouse HRP and scanned with C280 imaging systems (Azure Biosystems). ImageJ software was used to determine protein signal densities, which were subsequently normalized to corresponding β-actin signal densities.

Transthoracic echocardiography

Echocardiography measurements were conducted in unconscious mice using an induction chamber with 3% isoflurane. Isoflurane was adjusted to 0.5-1.5% to maintain a target heart rate of 450 ± 50 BPM. Ultrasound scans were obtained with the Vevo2100 imaging system and MS550D probe at a center frequency of 40 MHz. M-mode tracings, mitral inflow, and tissue velocities were measured using pulsed wave Doppler and tissue Doppler modes. Measurements were taken from at least three consistent cardiac cycles within the target heart rate range. Mice were monitored for recovery after echocardiography.

RNAseq and proteomics analyses

RNA quality and quantity were evaluated using the Agilent Bioanalyzer (25). RNA sequencing was conducted following the TruSEQ mRNA-Seq library protocol and performed on the Illumina NovaSEQ6000 platform, as previously described (25). For analysis of RNAseq raw FASTQ files, the biojupies online RNA-Seq platform (https://maayanlab.cloud/biojupies) was utilized for pathway and upstream transcription factor (TF) analyses. The ENRICHR option available on the same platform (https://maayanlab.cloud/Enrichr/) was employed for upstream regulator analysis. The Enrichr-KG database contains gene set libraries, including GO pathways, KEGG analysis, REACTOME pathway analysis, and TRRUST transcription factor analysis, among others.

The mass spectrometry analysis was performed by the Mass Spectrometry Core in Research Resources Center of University of Illinois at Chicago. For the analyses, 9 samples (N=3 for control, DIO, and DIO *Nox2*-KO) at 100 µg each were subjected to tryptic digestion using the S-Trap Micro kit (ProtiFi, NY, USA). The digested proteins were labeled with TMT10plex Isobaric Label Reagent Set (Thermo Fisher, Waltham, MA), combined, and desalted using an Oasis PRiME HLB 96-well plate (Waters). The pooled TMT-labeled peptides were fractionated into 80 fractions using off-line high-pH reverse phase (HPRP) liquid chromatography with an XBridge BEH C18 Column, 130Å, 3.5 µm, 4.6 mm X 250 mm (Waters). Every 13th fraction was concatenated together, resulting in 12 concatenated fractions that were dried and resuspended for LC-MS analysis. Approximately 1 µg of concatenated HPRP fractions were analyzed using a Q Exactive HF mass spectrometer coupled with an UltiMate 3000 RSLC nanosystem and a Nanospray Flex Ion Source. Digested peptides were separated on a Waters BEH C18 column at a flow rate of 300 nL/min using a gradient of 0.05% trifluoroacetic acid in H_2O, solvent A and 0.05% TFA acid in acetonitrile, solvent B. Full MS scans (resolution: 120,000) were acquired over an m/z range of 350-1400, and the 15 most intense peaks were fragmented for tandem mass spectra (resolution: 60,000). Ion selection thresholds and maximum allowed ion injection times were set for both full scans and fragment ion scans. Spectra were searched against the UniProt mouse database using Mascot daemon (2.6.0) with specified parameters. The search results were analyzed using Scaffold Q+S software (v5.0.0) for compilation and normalization of spectral counts. TMT purity correction was applied. Protein identification filtering criteria included a 1% false discovery rate (FDR) and minimum peptide count. Acquired differentially expressed genes file was further analyzed using the biojupies online platform to look at pathway enrichment analyses and upstream regulators.

H2DCFDA staining of mouse atria cells and hiPSC-aCMs and ROS measurements

As previously described, we measured ROS levels using a well-established technique.[61, 63-65] Briefly, summarizing freshly isolated mouse LA and RA cells and hiPSC-aCMs in Tyrode solution

(mM: NaCl 140, KCl 5.4, CaCl2 1, MgCl2 1, Glucose 5.5, Hepes 10, pH 7.4) were incubated for 30 min at 37°C with 10 μM 29,79-dichlorofluoresceindiacetate (DCFH-DA). DCFH-DA, being nonpolar, readily diffuses into cells, where it is hydrolyzed to the nonfluorescent polar derivative DCFH, thereby trapped within the cells. In the presence of ROS, DCFH is oxidized to the highly fluorescent 29,79-dichlorofluorescein (DCF). Extracellular DCFH-DA was washed out, and DCF fluorescence measurements were taken at room temperature in a Zeiss LSM 710 confocal microscope. Cells were excited with low laser power at 480 nm, and the emitted fluorescence was recorded at 610 nm with 400 ms scans every 3 minutes. The rate of ROS production during 12 min was obtained from the fitting of a linear regression to the DCF/min slope (GraphPad Prism).

SiRNA KD experiments

Mature hiPSC-aCMs were treated with either scrambled or PITX2-specific siRNAs (#SR321325B, 10 pmol) using Lipofectamine RNAiMAX (Invitrogen, Carlsbad, CA).[68] Stock solutions of both lipofectamine and SiRNA, prepared at 10 μM, were initially diluted in Opti-MEM medium. These solutions were then mixed at a 1:1 ratio and allowed to incubate for 5 minutes to form the siRNA-lipid complex. This complex was subsequently added to the cells dropwise and the cells were incubated for 2 days, after which the media was replaced (68). Following a recovery period of 2 days, the transfected cells were treated with either BSA or PA for a period of 5 days. *Data Analysis and Statistics*

Data are presented as mean ± SD unless otherwise specified. Significance is denoted as *P < 0.05, **P < 0.01, ***P < 0.001, ****P < 0.0001, with P < 0.05 considered significant. Statistical analyses include nonparametric unpaired and 2-tailed Mann-Whitney U test for data with normal distribution, and either 1-way or 2-way ANOVA with post hoc Bonferroni's corrections for multiple groups. Skewed data are expressed as medians with the first and third quartiles. Continuous variables are evaluated using unpaired Student's t-test or ANOVA, while categorical data are compared using Fisher's Exact test (9,25).

Study Approval

To collect human atrial tisse from different cardiac surgery patients, we used the UIC Institutional Review Board–approved protocol to enroll participants following receipt of informed written consent. Mouse studies were conducted as per previously approved Animal Care and Use (ACC) protocols approved by the Office of Animal Care and Institutional Biosafety (OACIB), UIC.

Data availabilty.

Data are available in public repositories, supporting XLS data values files; or from the corresssponding author upon request. The RNA-Seq and proteomics data reported in this manuscript were deposited into the National Center for Biotechnology Information's Gene Expression Omnibus database with the accession number GSE271748.

AUTHOR CONTRIBUTIONS

AS, **JD**, **HC**, **MAP**, and **DD** designed the experiments. **AS** was responsible for generating and maintaining different mouse strains, conducting iPSC culture and iPSC-aCM differentiation, applying fatty acid treatment, and performing RNA isolation and sample prep for RT-PCR and RNA-Seq, RT-PCR, Western blots, optical voltage mapping, and data analysis. **AS** also wrote the manuscript and performed and interpreted the RNA-Seq analysis using biojupies software. **JD** conducted EP whole-cell current-clamp recordings and calcium transient measurements on both mouse atrial CMs and iPSC-aCMs, and together with AS, performed ROS measurements on these cells. **MAP** assisted with EP whole-cell voltage-clamp recordings and analyzed the data. **HC**, along with **AO** and **MB**, assisted with iPSC line generation, aCM differentiation, and optical voltage mapping measurements. **HC** also performed flow cytometry on differentiated iPSC-aCMs. **OL** assisted with recruiting cardiac surgery patients for atrial tissue and conducted RT-PCR

on iPSC-aCMs. **JJ** performed mouse echocardiography across all mouse groups. SBN analyzed proteomics data in atrial lysates of different mouse groups. **KA**, **MM**, and **LER** provided HAT and whole blood for PBMC extraction. **DD** supervised the experiments and provided funding support, in addition to offering critical revisions of the manuscript. **SGO** and **JR** also contributed critical revisions to the manuscript. All authors provided critical feedback and contributed to the final manuscript.

ACKOWLEDGMENTS

Mouse atrial samples were sectioned and stained at the University of Illinois at Chicago Research Histology Core (RHC). We thank Peter Toth and Ke Ma from the University of Illinois at Chicago Fluorescence Imaging Core for their assistance in confocal microscopy. Mass spectrometry and proteomics on mouse atrial lysates was performed at the University of Illinois at Chicago Research Mass Spectrometry Core. RNA sequencing on iPSC-aCMs was performed at the University of Chicago Genomics Facility. This work was supported by VA Merit Award IO1BX004268 (PI: Darbar) NIH R01 HL138737 (PI: Darbar) NIH T32 HL139439 (PI: Darbar)

GRAPHICAL ABSTRACT

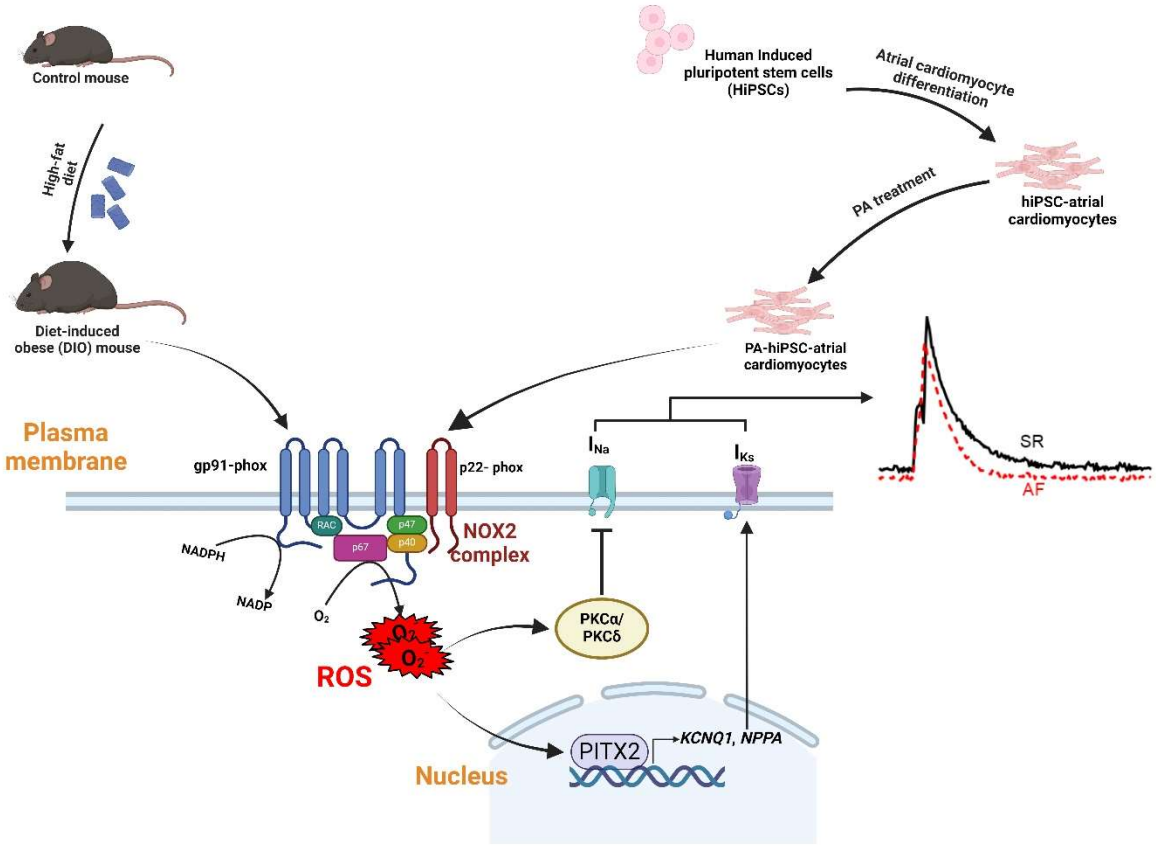

Increased NOX2 expression modulates ion channel remodeling via Pitx2 upregulation in obesity-mediated AF in diet-induced obese (DIO) mice and palmitic acid-treated hiPSC-aCMs

FIGURES AND LEGENDS

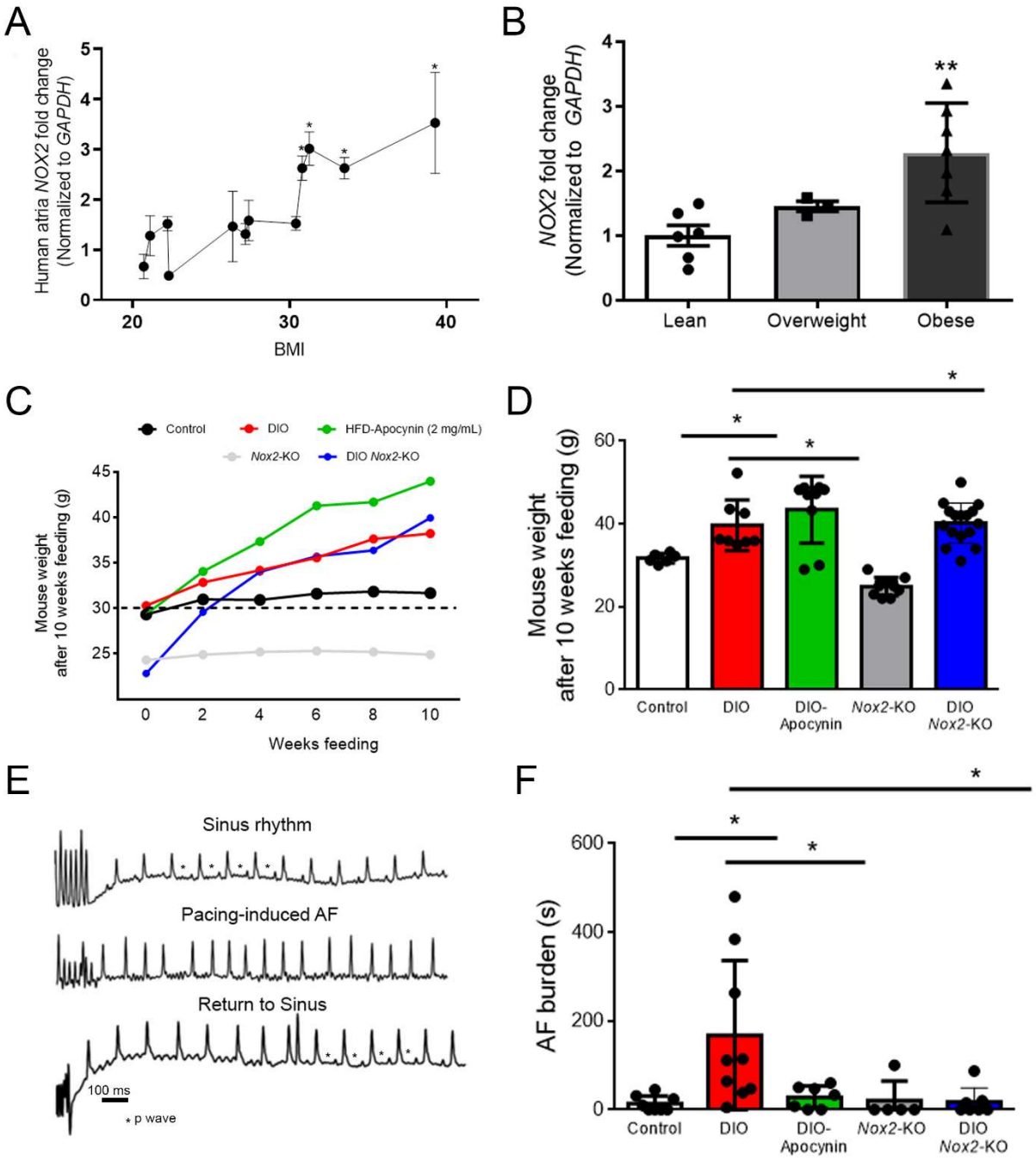

Figure 1. Genetic and pharmacologic inhibition of NADPH oxidase 2 (NOX2) reduces obesity-mediated atrial fibrillation (AF). (**A**) Human *NOX2* mRNA expression versus patient body mass index

(BMI kg/m^2). (**B**) Human *NOX2* mRNA expression in lean (N=6), overweight (N=3), obese individuals (N=7). (**C)** Average weight (g) of control, diet-induced obese (DIO), DIO-Apocynin, *Nox2*-knockout (KO), and DIO *Nox2*-KO mice over 10-week duration with a high-fat diet (HFD). **(D**) Final weights (g) of all five groups of mice after 10 weeks of HFD. **(E**) Atrial electrograms showing sinus rhythm at baseline (**top**), pacing-induced AF in DIO mice (**middle**), and sinus rhythm restoration in DIO mice (**bottom**). **(F**) Pacing-induced AF burden (duration, s) in Control (N=8), DIO (N=9), DIO-Apocynin (N=7), *Nox2*-KO (N=5), and DIO-*Nox2*-KO (N=7) mice; P>0.05; *P<0.05; **P<0.01; ***P<0.001, by 2-tailed, unpaired Student's *t* test

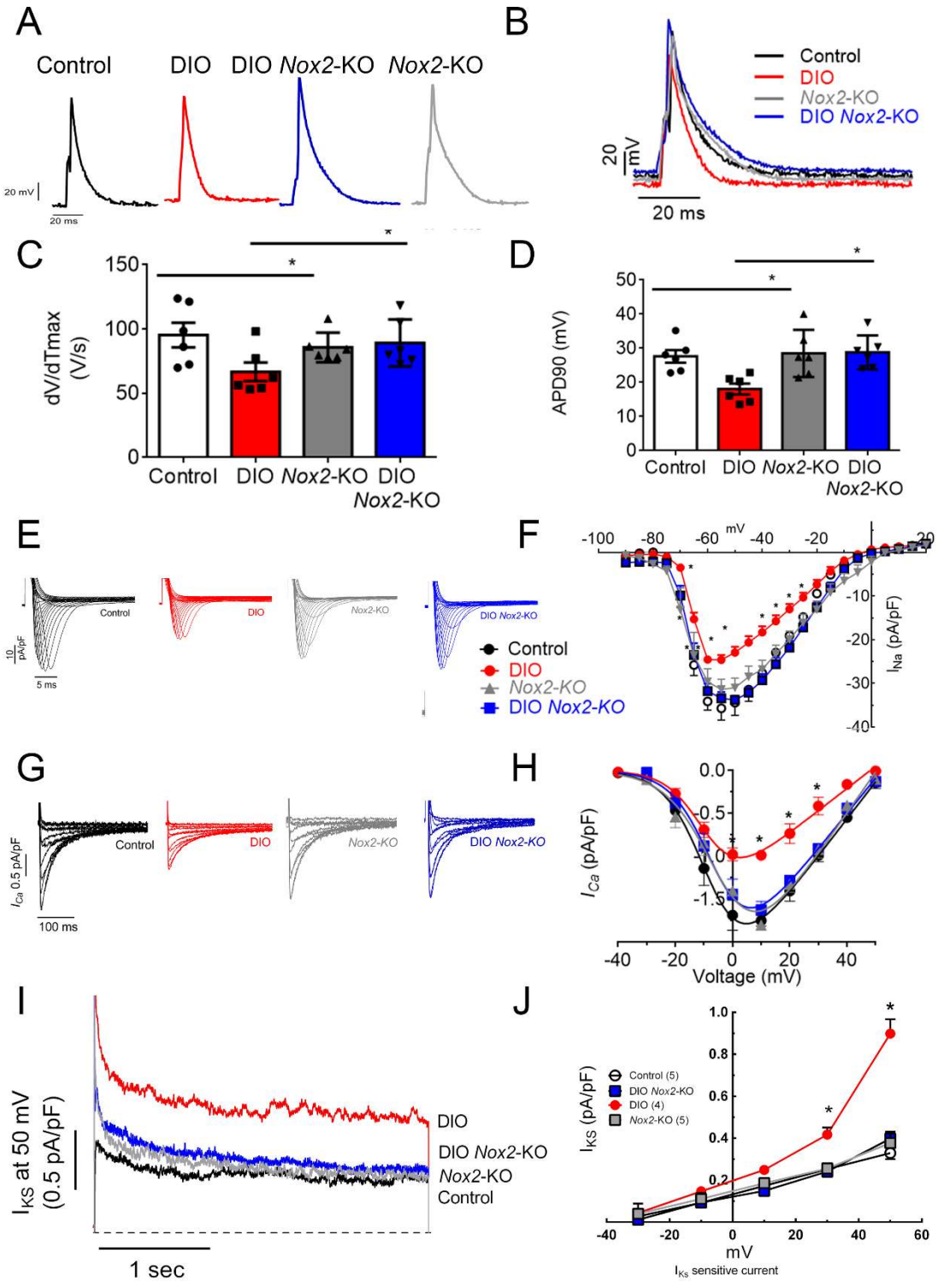

Figure 2. DIO *Nox2*-KO mice display increased atrial action potential (AP) and abrogation of obesity-induced ion channel remodeling. (**A-B**) Whole-cell patch-clamping of atrial myocytes of DIO-*Nox2*-KO mice showed increased prolongation of shortened AP duration (APD) caused by obesity. Representative

AP tracings in atrial myocytes in control (n=6 cells, N= 4 mice), DIO (n=6 cells, N= 4 mice), *Nox2*-KO (n=6 cells, N= 3 mice), and DIO-*Nox2*-KO mice (n=6 cells, N= 3 mice). (**C**) Instantaneous rate of voltage change over time (dV/dT_{max}), an indicator of atrial conduction velocity (CV; n=6 cells). (**D**) Measured APD at 90% repolarization (APD90; n=6 cells). (**E**) Representative sodium current (I_{Na}) tracings from control, DIO, and DIO-*Nox2*-KO mice showing increased currents in DIO-*Nox2*-KO atrial myocytes (n=6 atrial cells, N= 3 mice). (**F**) I_{Na} and voltage relationship (I-V curves) in control (N=6), DIO (N=6), and DIO-*Nox2*-KO mice (N=6). (**G)** Representative L-type calcium current ($I_{Ca,L}$) tracings from control, DIO, and DIO-*Nox2*-KO mice showing increased currents in DIO *Nox2*-KO atrial myocytes (n=4 cells, N= 3 mice). **(H)** $I_{Ca,L}$ and voltage relationship (I-V curves) in control (n=4), DIO (n=4), *Nox2*-KO (n=4), and DIO-*Nox2*-KO mice (n=4) (**I)** Slow delayed rectifier potassium current (I_{Ks}, treated with 1 μM HMR-1556) and voltage relationship (I-V curves) in control (n=5 cells, N=3 mice), DIO (n= 4 cells , N= 3 mice), *Nox2*-KO (n= 7 cells, N= 3 mice), and DIO-*Nox2*-KO mice (n= 8 cells , N= 3 mice) (**J)** Comparison of I_{Ks} at 50 mV in control (n=5 cells), DIO (n=4 cells), *Nox2*-KO (n= 7 cells), and DIO-*Nox2*-KO mice (n=8 cells)..; P>0.05; *P<0.05; **P<0.01; ***P<0.001;****P<0.0001 , by 1-tailed ANOVA test along with bonferroni post hoc test for multiple comparisons.

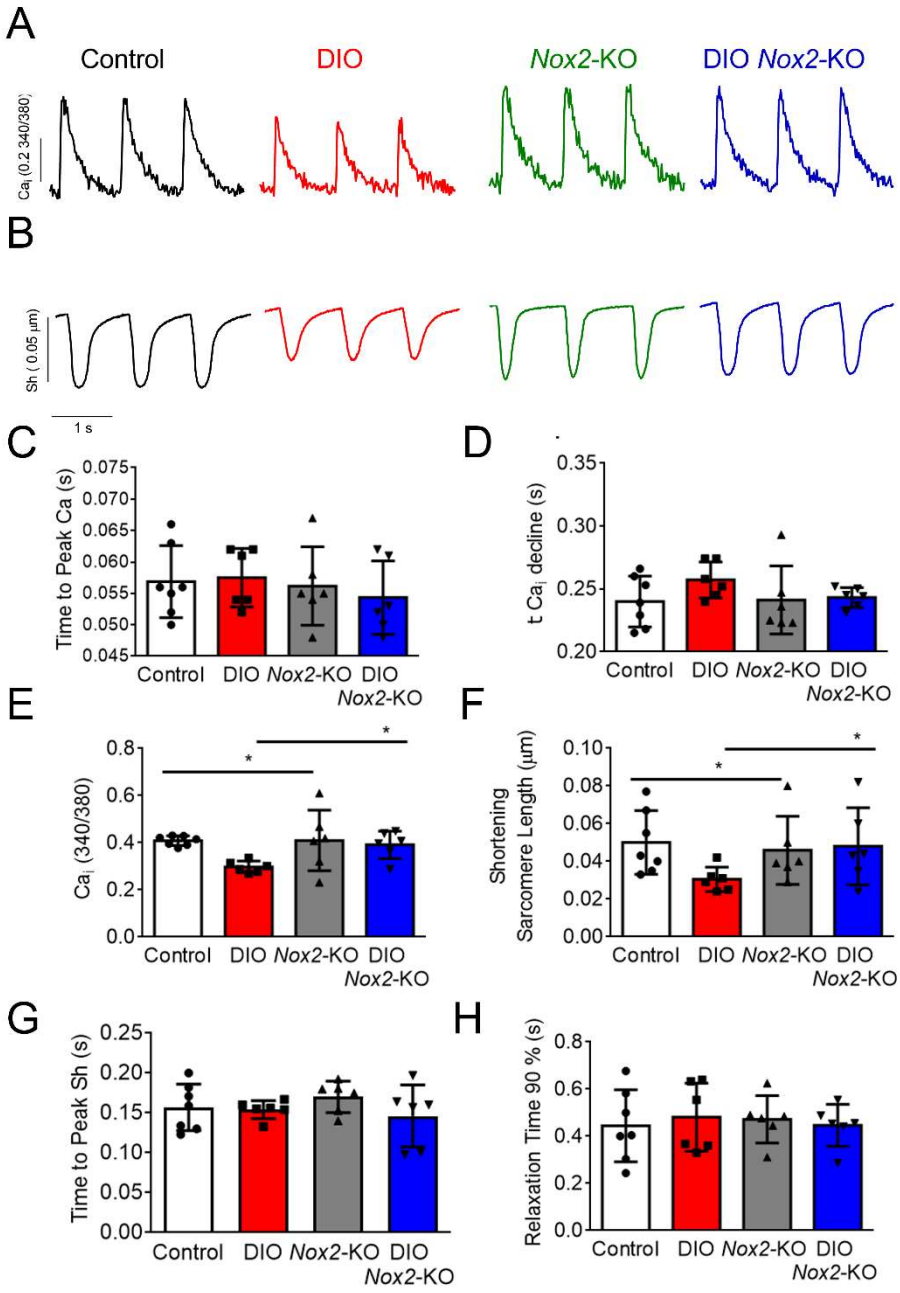

Figure 3. NOX2 inhibition improves atrial contractility in DIO mice. **(A)** Representative calcium transient tracings from control, DIO, *Nox2*-KO and DIO-*Nox2*-KO atrial myocytes. **(B)** Representative cell shortening tracings from control, DIO, *Nox2*-KO and DIO-*Nox2*-KO atrial myocytes; (n=6 cells, N= 3 mice each). (**C-E**) Quantification of calcium transient tracings- **(C)** time to peak calcium; **(D)** time for calcium decline; **(E)** Calcium transient peak amplitudes;. (**F-H**) Quantification of sarcomere cell shortening tracings

– **(F)** Shortening sarcomeric length; **(G)** Time to peak cell shortening; **(H)** Time to 90% relaxation. (N=6 cells). *P<0.05; **P<0.01; ***P<0.001; ****P<0.0001, by 2-tailed, unpaired Student's *t* test.

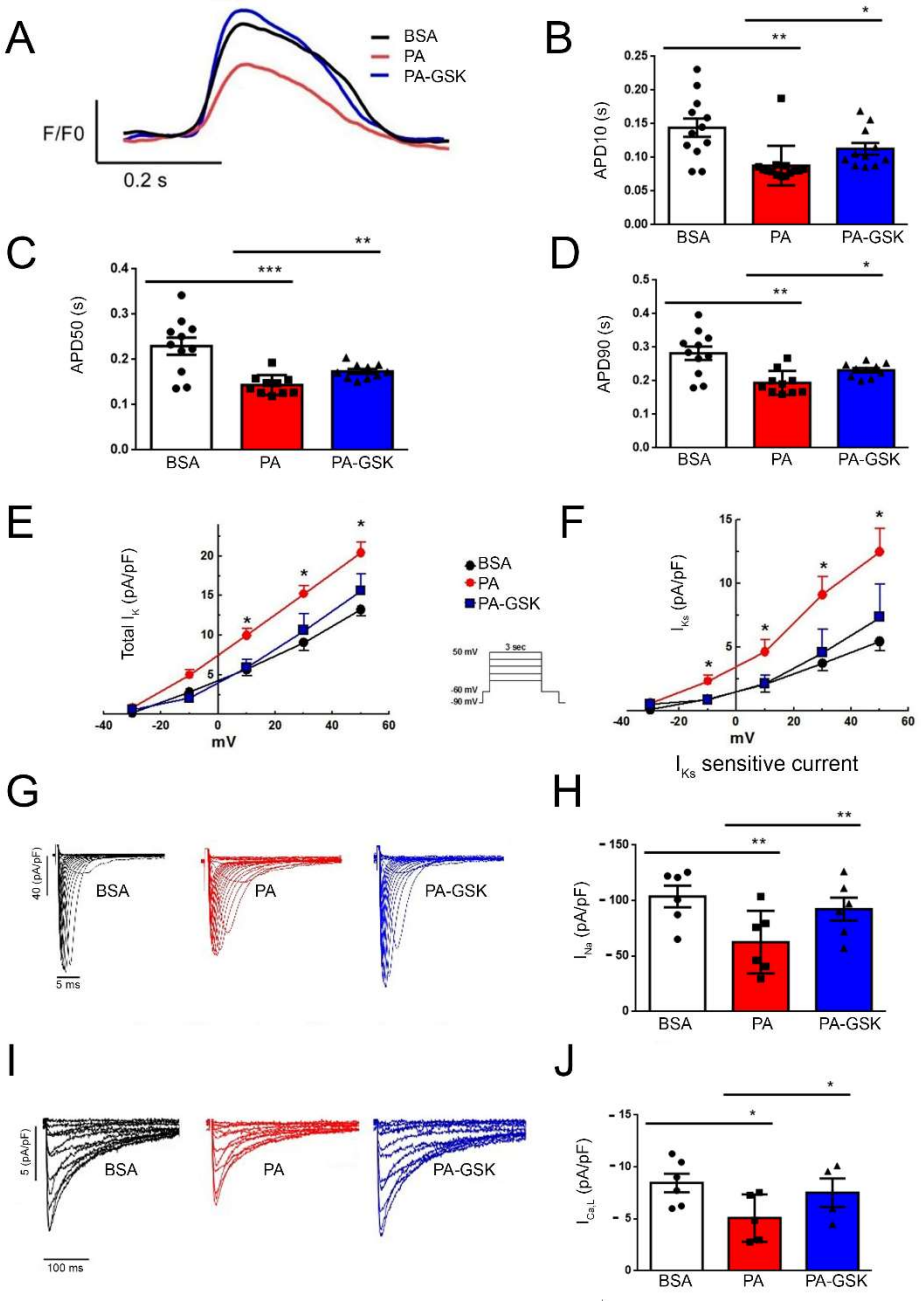

Figure 4. NOX2 inhibition in palmitic acid (PA) treated-hiPSC-aCMs using NOX2 small molecule inhibitor, GSK-2795039 reverses obesity-induced ion channel remodeling. (**A**) Optical voltage mapping on vehicle bovine serum albumin (BSA), PA, and PA-GSK-hiPSC-aCMs showed that the shortening of atrial action potential (AP) duration observed in PA-hIPSC-aCMs is abrogated in PA-GSK-hiPSC-aCMs. (**B**) Measured APD at 10% repolarization (APD10). (**C**) Measured APD at 50% repolarization

(APD50). (**D**) Measured APD at 90% repolarization (APD90). (**E)** Total potassium current (I_K) and voltage relationship (I-V curves) in BSA (N=5), PA (N=4), and PA-GSK-hiPSC-aCMs (N=3). (**F)** Slow delayed rectifier potassium current (I_{Ks}) and voltage relationship (I-V curves) in BSA (N=5), PA (N=4), and PA-GSK-hiPSC-aCMs (N=3) . **(G)** Representative I_{Na} traces in BSA (N=6), PA (N=6), and PA-GSK-hiPSC-aCMs (N=6). (**H)** Peak I_{Na} current density in BSA (N=6), PA (N=4), and PA-GSK-hiPSC-aCMs (N=3). **(I)** Representative $I_{Ca,L}$ traces in BSA (N=6), PA (N=6), and PA-GSK-hiPSC-aCMs (N=6). (**J)** Peak $I_{Ca,L}$ current density in BSA (N=6), PA (N=5), and PA-GSK-hiPSC-aCMs (N=4).). *P<0.05; **P<0.01; ***P<0.001; ****P<0.0001, by 1-tailed ANOVA test along with bonferroni post hoc test for multiple comparisons..

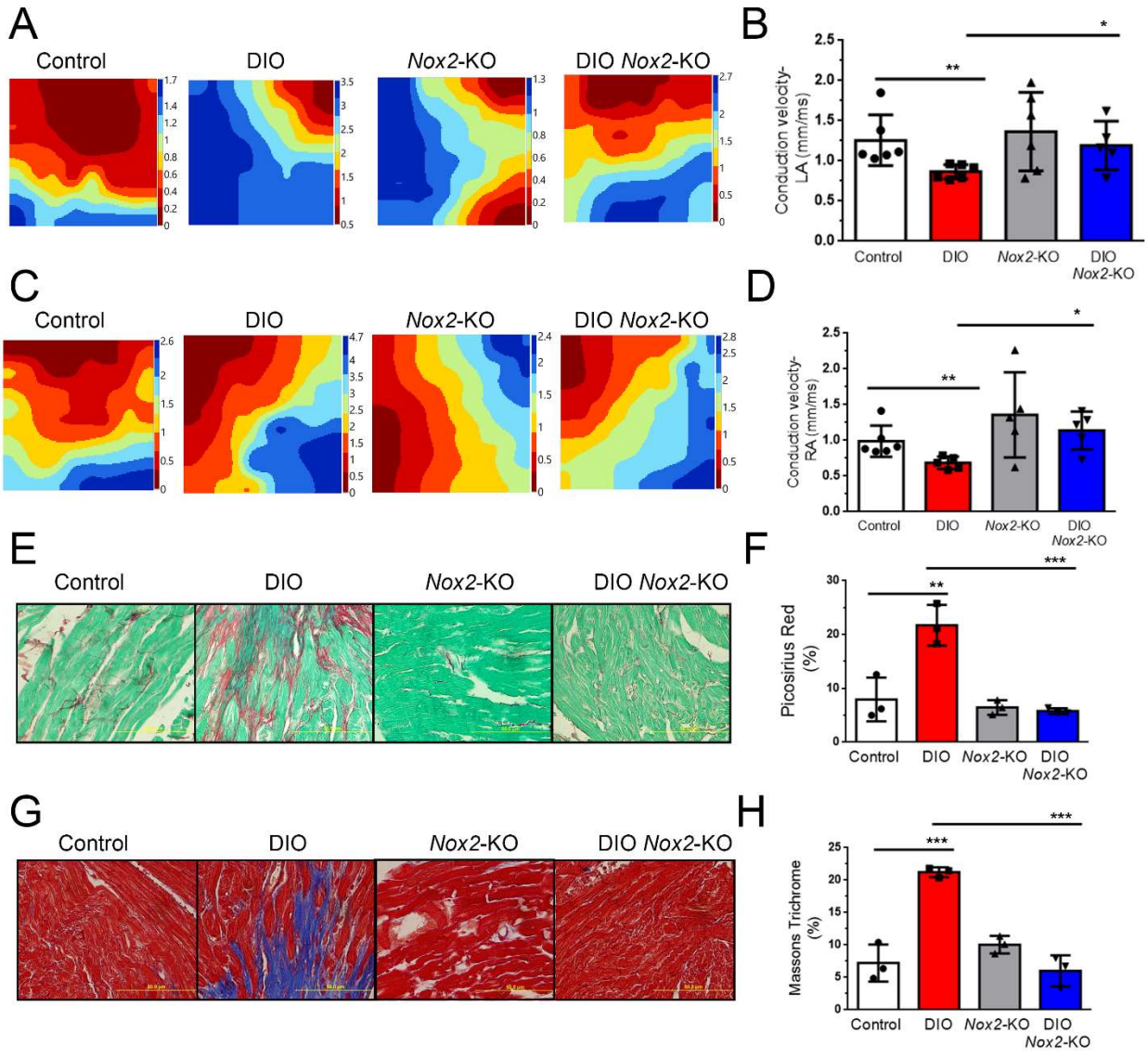

Figure 5. NOX2 inhibition prevents atrial fibrosis and increases atrial CV in DIO mice. (A) Representative left atrial (LA) isochronal maps of the 3 groups of mice using electrical mapping. **(B)** Quantification of mean left atrial (LA) CV in Control (N=6), DIO (N=6), *Nox2*-KO (N=5), and DIO-*Nox2*-KO mice (N=6). **(C)** Representative isochronal maps of the right atria (RA) in the 3 groups of mice using electrical mapping. **(D)** Quantification of mean right atrial (RA) CV in Control (N=6), DIO (N=6), *Nox2*-KO (N=5), and DIO-*Nox2*-KO mice (N=6). **(E)** Picosirius red staining of atrial myocytes from control, DIO, *Nox2*-KO and DIO-*Nox2*-KO. **(F)** Change in fibrosis (%) in the 3 groups of mice showing a significant reduction in fibrosis in DIO-*Nox2*-KO compared to DIO mice (N= 3 mice each). **(G)** Masson trichrome staining of atrial myocytes from control, DIO, and DIO-*Nox2*-KO. **(H)** Change in fibrosis (%) in the 4 groups of mice showing

a significant reduction in fibrosis in DIO-*Nox2*-KO compared to DIO mice (N=3 mice each). *P<0.05; **P<0.01; ***P<0.001; ****P<0.0001, by 2-tailed, unpaired Student's *t* test.

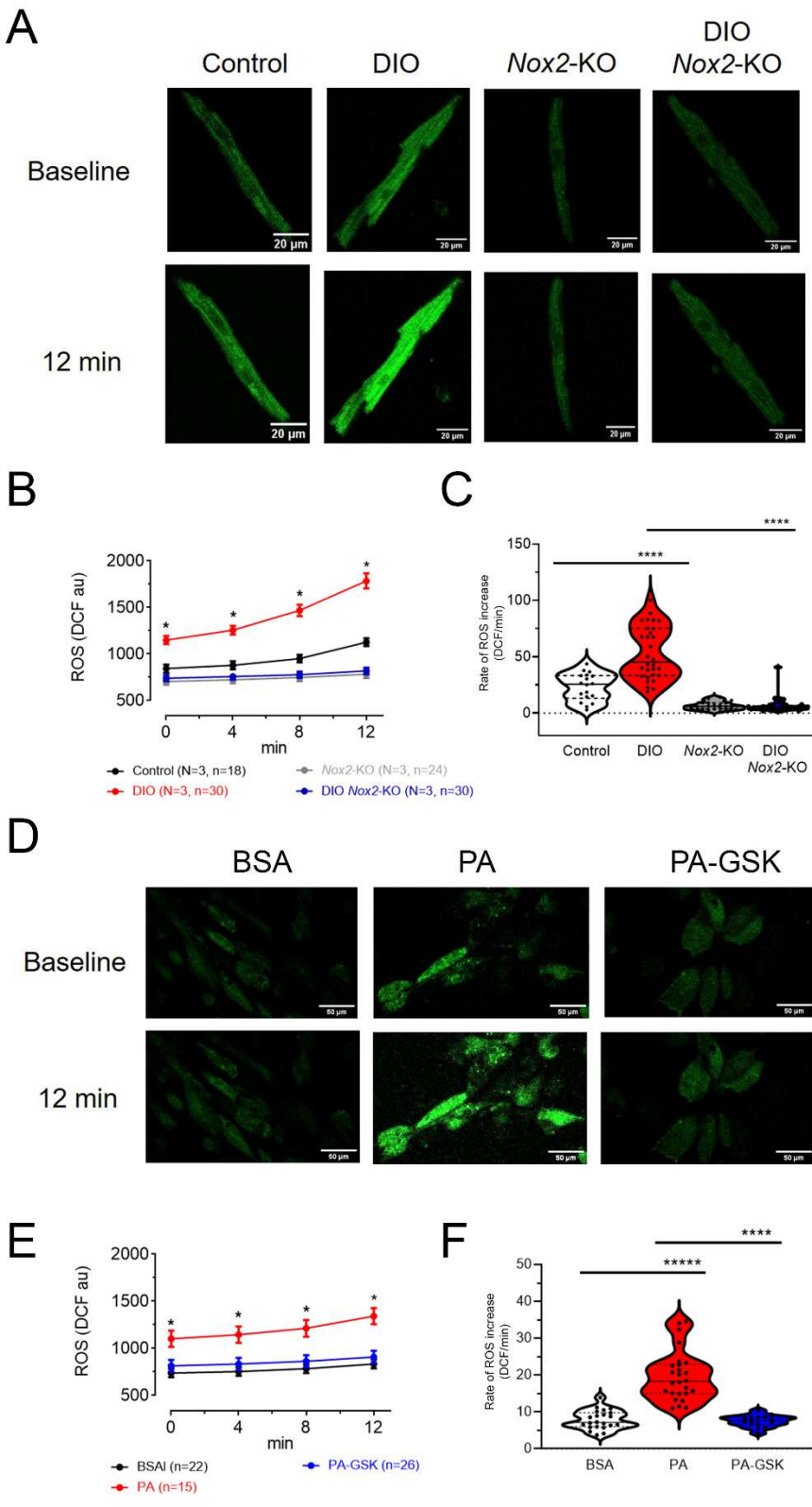
A
Control
DIO
Nox2-KO
DIO Nox2-KO
Baseline
12 min
20 µm
B
ROS (DCF au)
2000
1500
1000
500
0
4
8
12
min
Control (N=3, n=18)
DIO (N=3, n=30)
Nox2-KO (N=3, n=24)
DIO Nox2-KO (N=3, n=30)
C
Rate of ROS increase (DCF/min)
150
100
50
0
****
Control
DIO
Nox2-KO
DIO Nox2-KO
D
BSA
PA
PA-GSK
Baseline
12 min
50 µm
E
ROS (DCF au)
2000
1500
1000
500
0
4
8
12
min
BSAl (n=22)
PA (n=15)
PA-GSK (n=26)
F
Rate of ROS increase (DCF/min)
50
40
30
20
10
0
****
*****
BSA
PA
PA-GSK

Figure 6. NOX2 inhibition in palmitic acid (PA) treated-hiPSC-aCMs using NOX2 small molecule inhibitor, GSK-2795039 reverses obesity-induced ion channel remodeling. (**A**) Representative H2DCF staining of atrial cells from Control, DIO, *Nox2*-KO, and DIO *Nox2*-KO mice. (**B**) Measured H2DCF fluorescence of atrial cells from Control (n=18 cells) , DIO (n=30 cells), *Nox2*-KO (n= 24 cells), and DIO *Nox2*-KO (n=24 cells) mice at 0, 4, 8, and 12 minutes. (**C**) Rate of H2DCF increase in atrial cells from the four mouse groups. (**D**) Representative H2DCF staining of BSA, PA, and PA-GSK-hiPSC-aCMs. (**E**) Measured H2DCF fluorescence of BSA (n=22 cells), PA (n=26 cells), and PA-GSK-hiPSC-aCMs (n=15 cells) at 0, 4, 8, and 12 minutes. (**F**) Rate of H2DCF increase in the three hiPSC-aCM groups. P>0.05; *P<0.05; **P<0.01; ***P<0.001; ****P<0.0001, by 2-tailed, unpaired Student's *t* test.

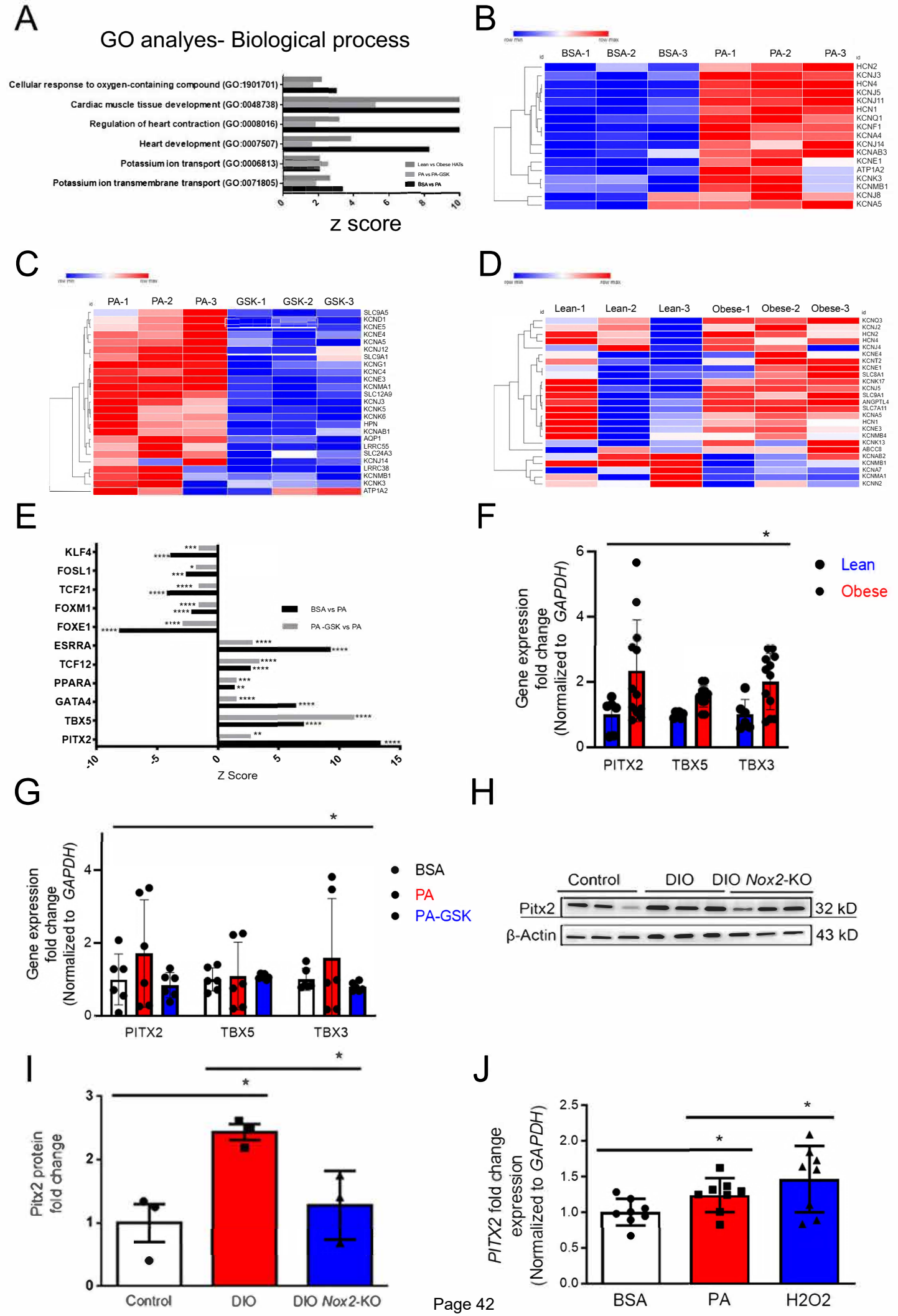
A
GO analyes- Biological process
Cellular response to oxygen-containing compound (GO:1901701)
Cardiac muscle tissue development (GO:0048738)
Regulation of heart contraction (GO:0008016)
Heart development (GO:0007507)
Potassium ion transport (GO:0006813)
Potassium ion transmembrane transport (GO:0071805)
Lean vs Obese HATs
PA vs PA-GSK
BSA vs PA
0 2 4 6 8 10
z score
B
BSA-1 BSA-2 BSA-3 PA-1 PA-2 PA-3
HCN2 KCNJ3 HCN4 KCNJ5 KCNJ11 HCN1 KCNQ1 KCNF1 KCNA4 KCNJ14 KCNAB3 KCNE1 ATP1A2 KCNK3 KCNMB1 KCNJ8 KCNA5
C
PA-1 PA-2 PA-3 GSK-1 GSK-2 GSK-3
SLC9A5 KCND1 KCNE5 KCNE4 KCNA5 KCNJ12 SLC9A1 KCNG1 KCNC4 KCNE3 KCNMA1 SLC12A9 KCNJ3 KCNK5 KCNK6 HPN KCNAB1 AQP1 LRRC55 SLC24A3 KCNJ14 LRRC38 KCNMB1 KCNK3 ATP1A2
D
Lean-1 Lean-2 Lean-3 Obese-1 Obese-2 Obese-3
KCNQ3 KCNJ2 HCN2 HCN4 KCNJ14 KCNE4 KCNT2 KCNE1 SLC8A1 KCNK17 KCNJ5 SLC9A1 ANGPTL4 SLC7A11 KCNA5 HCN1 KCNE3 KCNMB4 KCNK13 ABCC8 KCNAB2 KCNMB1 KCNA7 KCNMA1 KCNN2
E
KLF4 FOSL1 TCF21 FOXM1 FOXE1 ESRRA TCF12 PPARA GATA4 TBX5 PITX2
BSA vs PA
PA -GSK vs PA
-10 -5 0 5 10 15
Z Score
F
Gene expression fold change (Normalized to GAPDH)
Lean
Obese
PITX2 TBX5 TBX3
G
Gene expression fold change (Normalized to GAPDH)
BSA
PA
PA-GSK
PITX2 TBX5 TBX3
H
Control DIO DIO Nox2-KO
Pitx2 32 kD
β-Actin 43 kD
I
Pitx2 protein fold change
Control DIO DIO Nox2-KO
J
PITX2 fold change expression (Normalized to GAPDH)
BSA PA H2O2

Figure 7. Transcriptomic and pathway enrichment analysis in bovine serum albumin (BSA), palmitic acid (PA), and PA-GSK-hiPSC-aCMs and lean and obese human atrial tissues (HAT). (**A**) Common biological processes gene ontology pathways between the 3 comparisons. (**B**–**D**) Heatmaps of top upregulated and downregulated differentially expressed genes (DEGs) associated with the key GO pathway - Potassium transmembrane transport heart contraction (GO0071805) in (B) BSA vs PA-hiPSC-aCMs and (C) PA vs PA-GSK and hiPSC--aCMs and (D) Lean vs Obese HAT. (**E**) Common upregulated and downregulated cardiac related transcription factors in hIPSC-aCMs. (**F-G**) qPCR validation of *PITX2*, *TBX5*, and *TBX3* genes in both hIPSC-aCMs (N=3 each group) and HAT (N=3 for lean, N=6 for obese). (**H-I**) Pitx2 protein quantification using western blotting in control, DIO, and DIO *Nox2*-KO mice. (**J**) *PITX2* qPCR quantification on BSA, PA, and H2O2-hiPSC-aCMs (N=8 each group) (25 μM). *P<0.05; **P<0.01; ****P<0.0001, by 2-tailed, unpaired Student's *t* test and 1-tailed ANOVA with Tukey's multiple-comparison test**..**

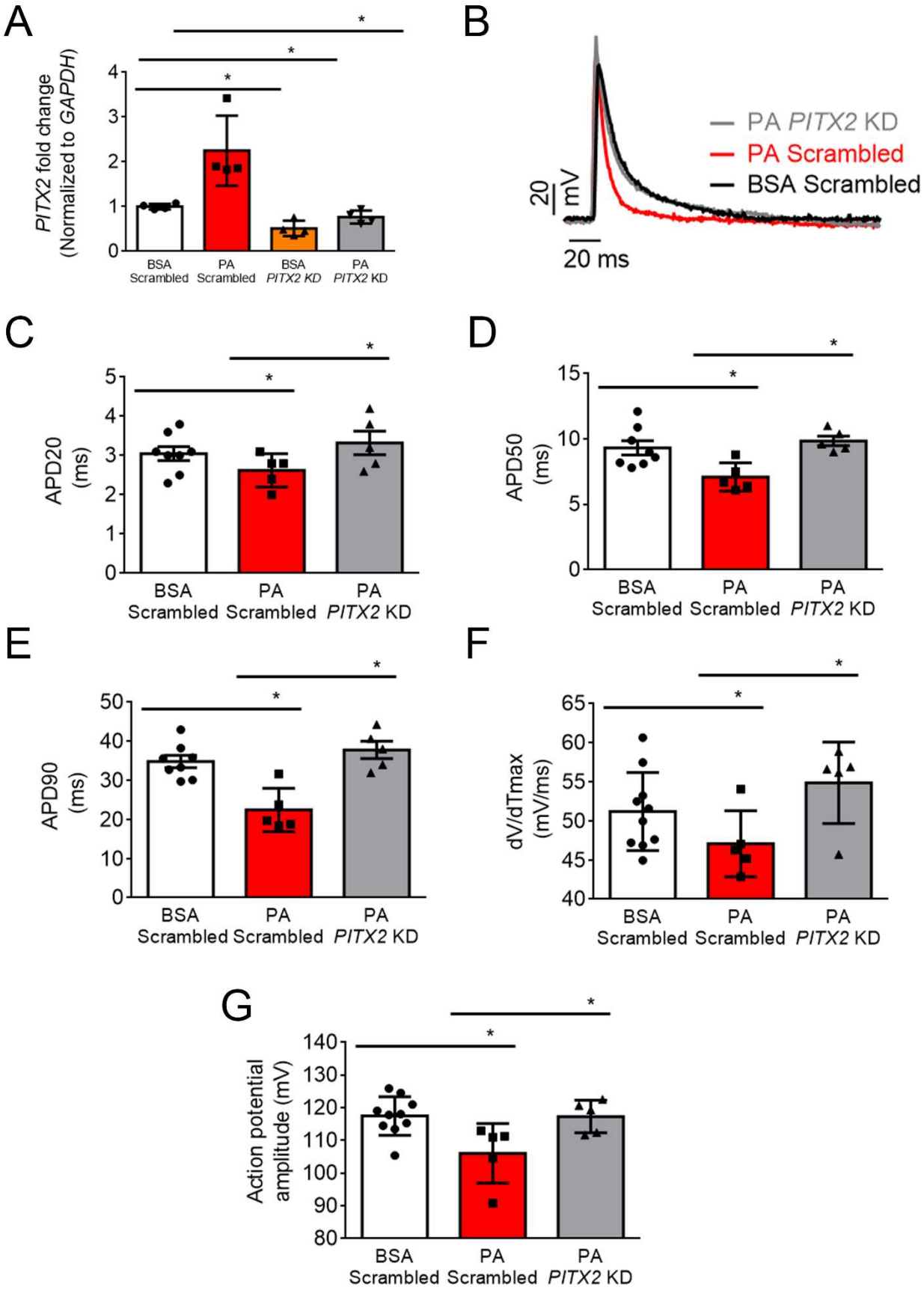

BSA - Bovine Serum Albumin PA- Palmitic acid KD- Knockdown

Figure 8. siRNA knockdown (KD) of PITX2 abrogates the effect of palmitic acid (PA) on hiPSC-aCMs: (**A**) *PITX2* expression in BSA scrambled, PA scrambled, BSA *PITX2* KD, and PA *PITX2* KD hiPSC-aCMs (n= 4 each). (**B**) Whole-cell patch-clamping of BSA scrambled (n=10), PA scrambled (n=5), and PA *PITX2* KD hiPSC-aCMs (n=5). **(C)** Measured APD at 20% repolarization (APD20). **(D)** Measured APD at 50% repolarization (APD50). **(E)** Measured APD at 90% repolarization (APD90). **(F)** Instantaneous rate of voltage change over time (dV/dT_{max}), an indicator of atrial conduction velocity (CV). (**G)** Maximum atrial potential amplitude (APAmax). P>0.05; *P<0.05; **P<0.01; ***P<0.001; ****P<0.0001.

References

1. Morillo, C. A., Banerjee, A., Perel, P., Wood, D. & Jouven, X. Atrial fibrillation: the current epidemic. *J Geriatr Cardiol* **14**, 195-203 (2017).

2. Lavie, C. J., Pandey, A., Lau, D. H., Alpert, M. A. & Sanders, P. Obesity and Atrial Fibrillation Prevalence, Pathogenesis, and Prognosis. *J Am Coll Cardiol* **70**, 2022-2035 (2017).

3. Vyas, V. & Lambiase, P. Obesity and Atrial Fibrillation: Epidemiology, Pathophysiology and Novel Therapeutic Opportunities. *Arrhythmia & Electrophysiology Review* **8**, 28-36 (2019).

4. Chatterjee, N. A. *et al*. Genetic Obesity and the Risk of Atrial Fibrillation: Causal Estimates from Mendelian Randomization. *Circulation* **135**, 741-754 (2017).

5. Abed, H. S. *et al*. Effect of Weight Reduction and Cardiometabolic Risk Factor Management on Symptom Burden and Severity in Patients With Atrial Fibrillation: A Randomized Clinical Trial. JAMA : the journal of the American Medical Association 310, 2050-2060 (2013).

6. Hohl, M. *et al*. Concomitant Obesity and Metabolic Syndrome Add to the Atrial Arrhythmogenic Phenotype in Male Hypertensive Rats. *J Am Heart Assoc* **6**, e006717 (2017).

7. Ornelas-Loredo, A. et al. Association Between Obesity-Mediated Atrial Fibrillation and Therapy With Sodium Channel Blocker Antiarrhythmic Drugs. JAMA Cardiol 5, 57-64 (2020).

8. Shu H;Cheng J;Li N;Zhang Z;Nie J;Peng Y;Wang Y;Wang DW;Zhou N; Obesity and atrial fibrillation: A narrative review from arrhythmogenic mechanisms to clinical significance. *Cardiovascular diabetology*; 2023 Jul 29;22(1):192.

9. McCauley, M. D. et al. Ion Channel and Structural Remodeling in Obesity-Mediated Atrial Fibrillation. Circ Arrhythm Electrophysiol 13, e008296 (2020).

10. He, Y., Zhou, L., Fan, Z., Liu, S. & Fang, W. Palmitic acid, but not high-glucose, induced myocardial apoptosis is alleviated by N -acetylcysteine due to attenuated mitochondrial-derived ROS accumulation-induced endoplasmic reticulum stress. Cell Death & Disease 9, 1-15 (2018).

11. Peoples, J. N., Saraf, A., Ghazal, N., Pham, T. T. & Kwong, J. Q. Mitochondrial dysfunction and oxidative stress in heart disease. Exp Mol Med 51 (2019).

12. Shingu, Y. *et al*. Correlation between increased atrial expression of genes related to fatty acid metabolism and autophagy in patients with chronic atrial fibrillation. *PLoS One* **15** (2020).

13. Sirker, A., Zhang, M. & Shah, A. M. NADPH oxidases in cardiovascular disease: insights from in vivo models and clinical studies. *Basic Res Cardiol* **106**, 735-747 (2011).

14. Joseph, L. C. *et al*. Dietary Saturated Fat Promotes Arrhythmia by Activating NOX2 (NADPH Oxidase *Circ Arrhythm Electrophysiol* **12**, e007573 (2019).

15. Sovari, A. A. & Dudley, J., Samuel C. Reactive oxygen species-targeted therapeutic interventions for atrial fibrillation. *Frontiers in physiology* **3**, 311 (2012).

16. Hansen, S. S. *et al*. Overexpression of NOX2 Exacerbates AngII-Mediated Cardiac Dysfunction and Metabolic Remodelling. *Antioxidants (Basel)* **11**, 143 (2022).

17. Looi Y.H., Grieve D.J., Siva A., Walker S.J., Anilkumar N., Cave A.C. Involvement of Nox2 NADPH oxidase in adverse cardiac remodeling after myocardial infarction. *Hypertension.* 2008;**51**:319–325.

18. Mighiu AS;Recalde A;Ziberna K;Carnicer R;Tomek J;Bub G;Brewer AC;Verheule S;Shah AM;Simon JN;Casadei B; Inducibility, but not stability, of atrial fibrillation is increased by Nox2 overexpression in mice. *Cardiovascular research* 2021 Oct 1; **117(11)**: 2354–2364

19. Yoo, S. *et al*. Attenuation of Oxidative Injury With Targeted Expression of NADPH Oxidase 2 Short Hairpin RNA Prevents Onset and Maintenance of Electrical Remodeling in the Canine Atrium. *Circulation* **142**, 1261-1278 (2020).

20. Szyller, J., Jagielski, D. & Bil-Lula, I. Antioxidants in Arrhythmia Treatment—Still a Controversy? A Review of Selected Clinical and Laboratory Research. *Antioxidants (Basel)* **11**, 1109 (2022).

21. Steinhubl, S. R. Why have antioxidants failed in clinical trials? *Am J Cardiol* **101**, 14D-19D (2008).

22. Karakikes, I., Ameen, M., Termglinchan, V. & Wu, J. C. Human Induced Pluripotent Stem Cell-Derived Cardiomyocytes: Insights into Molecular, Cellular, and Functional Phenotypes. *Circ Res* **117**, 80-88 (2015).

23. Ly, O. T. *et al*. Mutant ANP induces mitochondrial and ion channel remodeling in a human iPSC–derived atrial fibrillation model. *JCI Insight* **7** (2022).

24. Hong, L. *et al*. Human induced pluripotent stem cell-derived atrial cardiomyocytes carrying an SCN5A mutation identify nitric oxide signaling as a mediator of atrial fibrillation. *Stem cell reports* **16**, 1542-1554 (2021).

25. Argenziano, M. *et al*. Electrophysiologic Characterization of Calcium Handling in Human Induced Pluripotent Stem Cell-Derived Atrial Cardiomyocytes. *Stem Cell Reports* **10**, 1867-1878 (2018).

26. Schulz, C., Lemoine, M. D., Mearini, G., Koivumäki, J., Sani, J., Schwedhelm, E., Kirchhof, P., Ghalawinji, A., Stoll, M., Hansen, A., Eschenhagen, T. & Christ, T. PITX2 Knockout Induces Key Findings of Electrical Remodeling as Seen in Persistent Atrial Fibrillation - PubMed. *Circulation. Arrhythmia and electrophysiology* **16,** (2023).

27. Bai, J., Gladding, P. A., Stiles, M. K., Fedorov, V. V. & Zhao, J. Ionic and cellular mechanisms underlying TBX5/PITX2 insufficiency-induced atrial fibrillation: Insights from mathematical models of human atrial cells. *Scientific Reports* **8,** (2018).

28. Qiu, J. *et al*. NADPH oxidase inhibitor apocynin prevents atrial remodeling in alloxan-induced diabetic rabbits. *Int J Cardiol* **221**, 812-819 (2016).

29. Trumbull, K. A. *et al*. Diapocynin and apocynin administration fails to significantly extend survival in G93A SOD1 ALS mice. *Neurobiol Dis* **45**, 137-144 (2012).

30. Zhang XJ;Li L;Wang AL;Guo HX;Zhao HP;Chi RF;Xu HY;Yang LG;Li B;Qin FZ;Wang JP; GSK2795039 prevents Rip1-Rip3-MLKL-mediated cardiomyocyte necroptosis in doxorubicin-induced heart failure through inhibition of NADPH oxidase-derived oxidative stress. *Toxicology and applied pharmacology* 2023 Mar 15;**463**:116412

31. Liu, M., Liu, H. & Dudley, S. Reactive Oxygen Species Originating From Mitochondria Regulate the Cardiac Sodium Channel. *Circulation research* **107**, 967-974 (2010)

32. 1.Liu M;Shi G;Yang KC;Gu L;Kanthasamy AG;Anantharam V;Dudley SC; Role of protein kinase C in metabolic regulation of the cardiac na+ channel. *Heart rhythm* 2017 Mar; **14(3**):440-447

33. Yang Z, Subati T, Kim K, Murphy MB, Dougherty OP, Christopher IL, Van Amburg JC, Woodall KK, Barnett JV, Murray KT. Natriuretic Peptide Oligomers Cause Proarrhythmic Metabolic and Electrophysiological Effects in Atrial Myocytes. Circ Arrhythm Electrophysiol. 2022 Mar;15(3):e010636. doi: 10.1161/CIRCEP.121.010636

34. Savio-Galimberti, Eleonora, MD, PhD & Darbar, D., MD. Atrial Fibrillation and SCN5A Variants. *Cardiac electrophysiology clinics* **6**, 741-748 (2014).

35. Darbar, D. *et al*. Cardiac sodium channel (SCN5A) variants associated with atrial fibrillation. *Circulation* **117**, 1927-1935 (2008).

36. Jansen, H. J., McRae, M. D., Mackasey, M. & Rose, R. A. Regional and temporal progression of atrial remodeling in angiotensin II mediated atrial fibrillation. *Frontiers in physiology* 2022 Nov 1; **13:**1021807.

37. Pérez-Hernández, Matamoros, Barana, Amorós, Gómez, Núñez, Sacristán, Pinto, Fernández-Avilés, Tamargo, Delpón & Caballero. Pitx2c increases in atrial myocytes from chronic atrial fibrillation patients enhancing IKs and decreasing ICa,L. *Cardiovascular Research* **109,** 431–441 (2015). 38. Li, Y. *et al*. Regulation of IKs Potassium Current by Isoproterenol in Adult Cardiomyocytes Requires Type 9 Adenylyl Cyclase. *Cells* **8**, 981 (2019).

38. Franco, D., Sedmera, D. & Lozano-Velasco, E. Multiple roles of pitx2 in cardiac development and disease. *Journal of cardiovascular development and disease* 2017 Dec; **4(4)**: 16.

39. Zafari, A. M. *et al*. Role of NADH/NADPH Oxidase–Derived H 2 O 2 in Angiotensin II–Induced Vascular Hypertrophy. *Hypertension (Dallas, Tex. 1979)* **32**, 488-495 (1998).

40. Chen, L., Sampson, K. J. & Kass, R. S. Cardiac Delayed Rectifier Potassium Channels in Health and Disease. *Card Electrophysiol Clin* **8**, 307-322 (2016).

41. Jeevaratnam, K., Chadda, K. R., Huang, C. L. -. & Camm, A. J. Cardiac Potassium Channels: Physiological Insights for Targeted Therapy. *Journal of Cardiovascular Pharmacology and Therapeutics* **23**, 119-129 (2018).

42. Feghaly, J., Zakka, P., London, B., MacRae, C. A. & Refaat, M. M. Genetics of Atrial Fibrillation. *Journal of the American Heart Association* **7**, e009884 (2018).

43. Menon, A. *et al*. Electrophysiologic and molecular mechanisms of a frameshift NPPA mutation linked with familial atrial fibrillation. *Journal of Molecular and Cellular Cardiology* **132**, 24-35 (2019).

44. Perrin, M. J. & Gollob, M. H. The role of atrial natriuretic peptide in modulating cardiac electrophysiology. *Heart Rhythm* **9**, 610-615 (2012).

45. Wu, C. *et al*. NOX4/Src regulates ANP secretion through activating ERK1/2 and Akt/GATA4 signaling in beating rat hypoxic atria. *Korean J Physiol Pharmacol* **25**, 159-166 (2021).

46. Pakiet, A. *et al*. The Effect of a High-Fat Diet on the Fatty Acid Composition in the Hearts of Mice. *Nutrients* **12** (2020).

47. Nguyen, S. *et al*. The Effects of Fatty Acid Composition on Cardiac Hypertrophy and Function in Mouse Models of Diet-Induced Obesity. *J Nutr Biochem* **46**, 137-142 (2017).

48. Granéli, C., Hicks, R., Brolén, G., Synnergren, J. & Sartipy, P. Diabetic Cardiomyopathy Modelling Using Induced Pluripotent Stem Cell Derived Cardiomyocytes: Recent Advances and Emerging Models. *Stem Cell Rev and Rep* **15**, 13-22 (2019).

49. Sirker, A. et al. Cell-specific effects of Nox2 on the acute and chronic response to myocardial infarction. Journal of molecular and cellular cardiology 98, 11-17 (2016).

50. Kuroda, J. *et al*. NADPH oxidase 4 (Nox4) is a major source of oxidative stress in the failing heart. *PNAS* **107**, 15565-15570 (2010).

51. Lu, G. *et al*. H2S inhibits angiotensin II-induced atrial Kv1.5 upregulation by attenuating Nox4-mediated ROS generation during atrial fibrillation. *Biochem Biophys Res Commun* **483**, 534-540 (2017).

51. Hafstad, A. D. *et al*. NADPH Oxidase 2 Mediates Myocardial Oxygen Wasting in Obesity. *Antioxidants (Basel)* **9**, 171 (2020).

53. Murdoch, C. E. *et al*. Role of endothelial Nox2 NADPH oxidase in angiotensin II-induced hypertension and vasomotor dysfunction. *Basic Res Cardiol* **106**, 527-538 (2011).

54. Nazarewicz, R. R., Dikalova, A. E., Bikineyeva, A. & Dikalov, S. I. Nox2 as a potential target of mitochondrial superoxide and its role in endothelial oxidative stress. *Am J Physiol Heart Circ Physiol* **305**, H1131-H1140 (2013).

55. Bertero, E. & Maack, C. Calcium Signaling and Reactive Oxygen Species in Mitochondria. *Circulation research* **122**, 1460-1478 (2018).

56. Nikolaienko, R., Bovo, E. & Zima, A. V. Redox Dependent Modifications of Ryanodine Receptor: Basic Mechanisms and Implications in Heart Diseases. *Front Physiol* **9**, 1775 (2018).

57. Luczak, E. D. & Anderson, M. E. CaMKII oxidative activation and the pathogenesis of cardiac disease. *J Mol Cell Cardiol* **0**, 112-116 (2014).

58. Mesubi, O. O. *et al*. Oxidized CaMKII and O-GlcNAcylation cause increased atrial fibrillation in diabetic mice by distinct mechanisms. *J Clin Invest* **131**, e95747, 95747 (2021).

59. Bendall, J. K., Cave, A. C., Heymes, C., Gall, N. & Shah, A. M. Pivotal role of a gp91(phox)-containing NADPH oxidase in angiotensin II-induced cardiac hypertrophy in mice. *Circulation (New York, N.Y.)* **105**, 293-296 (2002).

60. O'Connell TD, Rodrigo MC, Simpson PC. Isolation and culture of adult mouse cardiac myocytes. Methods in Molecular Biology, 2002, vol 357, 271-296.

61. DeSantiago J, Bare DJ, Varma D, Solaro RJ, Arora R, Banach K. Loss of p-21 activated kinase (Pak1) promotes atrial arrhythmic activity. Hearth Rhythm 2018 Aug; 15(8):1233-1241. PMID: 29625277

62. Davies, L. *et al*. Mkk4 Is a Negative Regulator of the Transforming Growth Factor Beta 1 Signaling Associated With Atrial Remodeling and Arrhythmogenesis With Age. *J Am Heart Assoc* **3**, e000340 (2014).

63. DeSantiago, J. *et al*. p21-Activated kinase1 (Pak1) is a negative regulator of NADPH-oxidase 2 in ventricular myocytes. *J Mol Cell Cardiol* **67**, 77-85 (2014).

64. Prosser, B. L., Ward, C. W. & Lederer, W. J. X-ROS signaling: rapid mechano-chemo transduction in heart. *Science* **333**, 1440-1445 (2011).

65. Prosser, B. L., Ward, C. W. & Lederer, W. J. X-ROS signalling is enhanced and graded by cyclic cardiomyocyte stretch. *Cardiovasc Res* **98**, 307-314 (2013).

66. Li, M., Rao, M., Chen, K., Zhou, J. & Song, J. Selection of reference genes for gene expression studies in heart failure for left and right ventricles. *Gene* **620**, 30 (2017).

67. Červenák, Z. *et al*. Normalization strategy for selection of reference genes for RT-qPCR analysis in left ventricles of failing human hearts. *BMC Cardiovasc Disord* **22**, 180 (2022).

68. Brown, G. E. *et al*. Engineered cocultures of iPSC-derived atrial cardiomyocytes and atrial fibroblasts for modeling atrial fibrillation.

69. Tulloch, N. L. *et al*. Growth of Engineered Human Myocardium With Mechanical Loading and Vascular Coculture. *Circ Res* **109**, 47 (2012).